Reconstruction Algorithm for Compressive Multiband Spectral Imaging Fusion based on Spectral Unmixing

Author

Edwin Mauricio Vargas Díaz

In fulfillment of the requirements for the degree of

Magister en Ingeniería Electrónica

Director

Henry Arguello Fuentes

Ph.D Electrical and Computer Engineering

University of Delaware

Universidad Industrial de Santander

Facultad de Ingenierías Físico-mecánicas

Escuela de Ingeniería Eléctrica, Electrónica y Telecomunicaciones

Maestría en Ingeniería Electrónica

Bucaramanga, 2018

Contents

Resumen

TÍTULO: Algoritmo de reconstrucción para la fusión de imágenes espectrales multibanda comprimidas basado en desmezclado espectral. [1]

AUTOR: Edwin Mauricio Vargas Díaz.[2]

PALABRAS CLAVE: Imágenes espectrales, muestreo compresivo, fusión de datos, muestreo remoto.

DESCRIPCIÓN:

En los últimos años, una forma común de mejorar la resolución espacial de imágenes hiper-espectrales (HS) ha sido la fusión con información complementaria proveniente de imágenes multiespectrales (MS) o pancromáticas. La imagen HS de alta resolución resultante permite aplicaciones en campos donde la adquisición de imágenes de alta resolución espectral y espacial es extremadamente costosa. Este trabajo propone un nuevo método para reconstruir una imagen de alta resolución espacial y alta resolución espectral a partir de medidas comprimidas adquiridas por múltiples sensores, cada uno con diferente resolución espacial y espectral, específicamente imágenes HS y MS comprimidas. Para resolver este problema, se introduce un modelo de fusión basado en el modelo de mezclas lineales clásicamente usado para imágenes HS. Además, se desarrolla un algoritmo de optimización basado en una estrategia de bloques coordenados descendiente. Las restricciones de no negatividad y suma a uno, resultantes de las propiedades físicas de las abundancias, y una penalización de variación total, son usadas para regularizar este problema inverso mal condicionado. Resultados de simulación para imágenes HS y MS reales comprimidas, muestran que el algoritmo propuesto puede proveer resultados de fusión que son muy cercanos a aquellos obtenidos con imágenes no comprimidas, con la ventaja de usar un número reducido de medidas.

[1] Trabajo de Investigación

[2] Escuela de ingenierías eléctrica, electrónica y telecomunicaciones, Universidad Industrial de Santander. Supervisor, Henry Arguello Fuentes.

Abstract

Title: Reconstruction Algorithm for Compressive Multiband Spectral Imaging Fusion based on Spectral Unmixing.[3]

Author: Edwin Mauricio Vargas Diaz.[4]

Keywords: Spectral Imaging, compressive sampling, data fusion, remote sensing.

In the last years, one common way of enhancing the spatial resolution of hyperspectral (HS) images has been to fuse this image with complementary information coming from multispectral (MS) or panchromatic images. The resultant high resolution HS image allows applications in fields where building a unique imaging system with high spectral and high spatial resolution requirements is extremely expensive. This work proposes a new method for reconstructing a high-spatial high-spectral image from measurements acquired after compressed sensing by multiple sensors of different spectral and spatial resolutions, with a specific attention to HS and MS compressed images. To solve this problem, we introduce a fusion model based on the linear spectral unmixing model classically used for HS images and investigate an optimization algorithm based on a block coordinate descent strategy. The non-negative and sum-to-one constraints resulting from the intrinsic physical properties of abundances as well as a total variation penalization are used to regularize this ill-posed inverse problem. Simulations results conducted on realistic compressed HS and MS images show that the proposed algorithm can provide fusion results that are very close to those obtained with uncompressed images, with the advantage of using a significant reduced number of measurements.

[3]Research work

[4]Escuela de ingenierías eléctrica, electrónica y telecomunicaciones, Universidad Industrial de Santander. Supervisor, Henry Arguello Fuentes.

Introduction

Hyperspectral (HS) sensors collect data that can be represented by a three-dimensional data cube [1]. This data cube referred to as HS image is a collection of 2D images, where each 2D image is captured at a specific wavelength. HS images are characterized by a high spectral resolution which allows an accurate identification of the different materials contained in the scene of interest. Analyzing the spectral information of HS images has allowed the development of many applications in the fields of remote sensing [2], medical imaging [3] or astronomy [4]. However, due to technological reasons, HS images are limited by their relatively low spatial resolution [5, 6, 7]. For instance, the Hyperion imaging spectrometer yields HS images with about 220 spectral bands, which extend from the visible region (0.4 to 0.7 μm) through the SWIR (about 2.5 μm), with a spatial resolution of 30 m by pixel [8] that can be insufficient for some practical applications.

In addition to their reduced spatial resolution, conventional spectral imaging devices have the drawback of requiring to scan a number of zones that grows linearly in proportion to the desired spatial or spectral resolutions. Finally, HS images require to acquire a large amount of data that must be stored and transmitted. To overcome this limitation, motivated by the compressed sensing (CS) theory [9], several compressive spectral imagers have been recently proposed [10, 11, 12]. Compressive spectral imaging (CSI) techniques [13, 14] exploit the fact that HS images are sparse in some basis and can thus be efficiently compressed by using CS. As a consequence, the images acquired with CSI have a reduced number of measurements when compared to conventional spectral imaging devices, which makes them attractive for many practical applications.

To overcome the spatial resolution limitation, a common trend is to fuse HS images with high spatially resolved sensors. For instance, the IKONOS satellite sensor can provided multispectral images with four bands (near-infrared, red, green and blue) and with a spatial resolution of 3.2 m [15] which is comparatively higher than HS sensors. A typical example studied in this work is the fusion of HS images (having high spectral resolution) with multispectral (MS) images (having high spatial resolution) [16, 17]. Another example is HS pansharpening, which addresses the fusion of panchromatic and HS images [18]. Many algorithms have been proposed in the literature for image fusion (see [18, 19] for recent reviews). Fast fusion algorithms based on spectral mixture analysis have been developed to fuse HS and MS images [20, 21]. The coupled nonnegative matrix factorization (CNMF) has also been recently proposed to estimate the endmember and abundance matrices using an alternating optimization method [22].

This research work investigates a new algorithm allowing the fusion of HS and MS images acquired with compressive spectral imagers using a sparse representation of abundance maps. The sparsity of abundance maps has already been exploited for image fusion. The compressive spectral fusion problem was recently investigated in [23] where the image of interest was decomposed in a fixed basis with a sparse representation. A related compressive fusion method based on a multiresolution analysis and a simple maximum selection fusion rule was previously proposed in [24], where the images to be fused were acquired in a single band with the same size. In this work, we consider CSI devices such as the Colored Coded Aperture Snapshot Spectral Imager (C-CASSI) and the Multiple Snapshot Spatial Spectral coded Compressive Spectral Imager (SSCSI), which sense multiple 2D coded projections of the underlying scene. More formally, the projections measured in C-CASSI and SSCSI systems can be written as $\mathbf{y} = \mathbf{H}\mathbf{f}$, where $\mathbf{f} \in \mathbb{R}^{N^2L}$ is a vector representation of the spatio-spectral 3-dimensional source $\boldsymbol{\mathcal{F}} \in \mathbb{R}^{N\times N\times L}$ ($N \times N$ is used for the spatial dimensions and L is the spectral dimension), and $\mathbf{H}$ is a matrix that is associated with the optical architecture of the spectral imagers. Note that the non-zero entries of $\mathbf{H}$ are determined by the colored coded aperture in the CASSI architecture [25] and by the coded mask in SSCSI [26]. Note also that these optical filters or coded apertures can be selected randomly or designed as in [27, 25, 28, 29].

The proposed fusion algorithm reconstructs the high-spatial high-spectral image represented by the vector $\mathbf{f} \in \mathbb{R}^{N^2L}$ from compressive measurements $\mathbf{y}_m$ and $\mathbf{y}_h$, resulting from HS and MS images concatenated in vectors $\mathbf{f}_m \in \mathbb{R}^{N^2L_m}$ and $\mathbf{f}_h \in \mathbb{R}^{N_h^2L}$. Note that the target image must have the high-spatial resolution of $\mathbf{f}_m$ and the high-spectral resolution of $\mathbf{f}_h$. The proposed algorithm is based on the linear mixture model, which assumes that each pixel of the target image is a linear mixture of spectral signatures (referred to as endmembers). Using the linear mixture model (LMM), an observation pixel $\mathbf{f}_j \in \mathbb{R}^L$ can be represented as $\mathbf{f}_j = \mathbf{M}\boldsymbol{\alpha}_j$, where $\mathbf{M} \in \mathbb{R}^{L\times p}$ is the endmember matrix whose columns are spectral signatures, p is the number of materials in the image (supposed to be known) and $\boldsymbol{\alpha}_j = [\alpha_{j1}, ..., \alpha_{jp}]^T \in \mathbb{R}^p$ contains the abundances of the jth pixel of the HS image (see [30] for details). As a consequence, the target high resolution HS image can be written as $\mathbf{f} = \overline{\mathbf{M}}\boldsymbol{\alpha}$, where $\overline{\mathbf{M}} = \mathbf{M} \otimes \mathbf{I}_{N^2}$, $\mathbf{I}_{N^2} \in \mathbb{R}^{N^2\times N^2}$ is the $N^2 \times N^2$ identity matrix, $\otimes$ is the Kronecker product, and $\boldsymbol{\alpha} = \text{vec}(\mathbf{A}^T) \in \mathbb{R}^{N^2p}$ is obtained by vectorizing the matrix $\mathbf{A} = [\boldsymbol{\alpha}_1, \cdots, \boldsymbol{\alpha}_{N^2}] \in \mathbb{R}^{p\times N^2}$ containing the abundances of all the image pixels. The procedure by which the spectrum of a pixel is decomposed in a set of endmembers and its corresponding abundance fractions under the LMM is well know as linear spectral unmixing (or spectral unmixing). It should be noted that spectral unmixing and therefore the LMM was already used for image fusion in recent works such as [21, 22]. However, these works did not take into account any compressive sensing operation (i.e., the matrices $\mathbf{H}_m$ and $\mathbf{H}_h$ were equal to the identity matrix), which is the main contribution of this thesis. In Fig. 1 is depicted an schematic representation of the problem of fusing HS and MS compressed images based on spectral unmixing which we aim to solve.

This work shows that acquiring images with CS and exploiting jointly the LMM for the unknown image of interest and the sparsity of abundance maps leads to efficient image fusion when compared to other existing approaches [21, 23, 24], even if the observed images have been compressed and acquired with reduced acquisition time. Note that standard endmember extraction algorithms, such as VCA [31], SVMAX [32] or N-FINDR [33], cannot be used directly when the observed images have been subjected to CS. This endmember extraction step is contained within the proposed fusion algorithm.

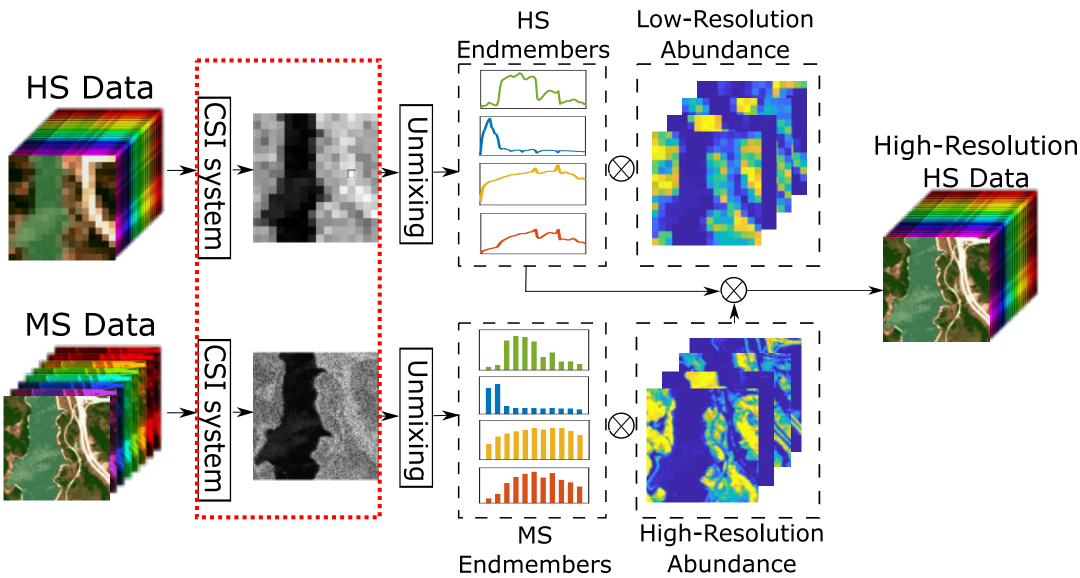

Figure 1: Schematic representation of the fusion problem addressed in this work.

1

Objectives

1.1 General Objective

To design an algorithm based on Spectral Unmixing to reconstruct a high-spatial high-spectral image from fusing a compressive low-spatial high-spectral image measurement and a compressive high-spatial low-spectral image measurement.

1.2 Specific objectives

- To develop a matrix model of the compressive hyperspectral image measurement and compressive multispectral image measurements which are intended to be fused.
- To formulate an optimization algorithm based on the linear spectral mixing model in order to fuse compressive measurements of HS and MS images.
- To design an iterative algorithm in order to recover the high-spatial high-spectral resolution image from compressive measurements.
- To validate the designed algorithm through simulations and, compare the reconstruction results with respect to the state-of-art fusion algorithms .

2

Theoretical Background

2.1 Spectral Imaging

The spectrum of a point in a scene is represented by the distribution of its electromagnetic radiation over a range of wavelengths. Since a huge amount of applications can be developed from detailed spectra, several acquisition systems for precise spectral measurements have been studied for decades. These include applications in the fields of remote sensing [2], medical imaging [3, 34], geology [35], biological science [36], scientific observation and many other fields [37]. The traditional sampling methods for HS imaging are based on measuring sequence of 2D images, which are then concatenated into a single data cube. For instance, push-broom spectral imaging sensors [38] capture a spectral cube with one focal plane array (FPA) measurement per spatial line of the scene [13], and whereas whisk-broom acquires a single spectral pixel at a time [39], and tunable filter imagers [40] measure 2D images at a specific wavelength. In all the traditional methods for HS data acquisition, due to technological reasons, there is a trade off between spectral and spatial resolution. Generally, HS images benefit from excellent spectroscopic properties with several or hundreds of thousands of contiguous bands but are limited by their relatively low spatial resolution [5]. For instance, the Hyperion imaging spectrometer yields HS images with about 220 spectral bands, which extend from the visible region (0.4 to 0.7 μm) through the SWIR (about 2.5 μm), with a spatial resolution of 30 m [8]. In addition to their reduced spatial resolution, conventional spectral imaging devices have the drawback of requiring to scan a number of zones that grow linearly in proportion to the desired spatial or spectral resolution. Finally, HS images require to acquire a large amount of data that must be stored and transmitted.

2.2 Compressive Spectral Imaging

Motivated by the development of compressed sensing theory (CS), more recent approaches to acquire spectral data have been proposed. CS relies on two principles: sparsity and incoherence [41]. Sparsity is related to the signals of interest and CSI exploits the fact that hyperspectral images can be sparsely represented in a proper basis Ψ. More formally, if we consider a hyperspectral image represented as a vector $\mathbf{f} \in \mathbb{R}^{N^2L}$, this can be expressed as $\mathbf{f} = \Psi\theta$, where θ is an S-sparse vector and $S \ll N^2L$. Incoherence relates to the sensing modality and expresses the idea that sparse vectors in Ψ must be spread out in the domain in which they are acquired [41]. There are mainly two approaches for compressing spectral data that have been implemented in practical applications: *i)* spatial coding based CS imagers, such as the coded aperture snapshot spectral imager (CASSI) [42], and *ii)* spatial and spectral coding-based spectral imagers, such as the spatio-spectral encoded compressive spectral imager (SSCSI) [43], or the Colored CASSI (C-CASSI) [25]. In this work, we focus on the second class which captures a spectral scene using a single or multiple 2D snapshots obtained with different sampling patterns. The next subsections describe, in detail, the mathematical model of C-CASSI and SSCSI. Note that these two architectures have been implemented in practical applications (based on spatial and spectral coding), which explains why they have been considered in our work. Even though only two CSI devices are considered, the techniques developed here might be extended to other architectures such as those studied in [11, 12, 29]. Note that the structure of the matrix $\mathbf{H}$ is related to the optical architecture of each implementation. Finally, it is worth noting that the matrices $\mathbf{H}_m$ and $\mathbf{H}_h$ which will be used later in section 4, correspond to MS and HS alternatives, and they are instances of the matrices $\mathbf{H}$ presented in this section.

2.2.1 Colored CASSI. The coded aperture snapshot spectral imager (CASSI) is one of the most representative CSI architectures, which comprises a dispersive element and a coded aperture [42]. The coded aperture is the spatial coding optical element defined as a block-unblock lithographic mask or a spatial light modulator (SLM) [13]. The CASSI architecture codifies the 3D data only in the spatial domain, i.e., each pixel of the coded aperture blocks or let pass the entire spectral information. The colored CASSI (C-CASSI) is a different variation of the CASSI system, which replaces the binary masks by multiple-patterned arrays of selectable optical filters or colored coded apertures to provide a richer modulation in both spatial and spectral domains [25]. In Figure 2.1 a colored coded aperture pattern is shown. Each pixel on the coded aperture is one of the possible optical filters whose spectral response can be selected. C-CASSI reduces the number of 2D measurements required to recover the underlying image due to the higher randomness of these 3D coded aperture structures. Note that the coded source is dispersed by a prism and that the coded and dispersed source is captured by a focal plane array (FPA). The sensing representation of the C-CASSI system is depicted in Fig 2.2. The ℓ-th intensity at the (i, j)-th pixel of the detector using a colored coded aperture $\mathbf{T}^{\ell}$ is

$$Y_{ij}^{\ell} = \sum_{k=0}^{L-1} \mathcal{F}_{i(j-k)k} T_{i(j-k)k}^{\ell} + \omega_{ij} \tag{2.1}$$

where $\boldsymbol{\mathcal{F}}$ is an $N \times N \times L$ spectral data cube, $T_{ijk}^{\ell} \in \{0, 1\}$ is the discretization of the ℓ-th colored coded aperture, ω_{ij} is the white Gaussian noise of the sensing system, and $\ell = 0, ..., K-1$ with $K \in \mathbb{N}$ representing the number of snapshots. Vectorizing the measurements $\mathbf{Y}_{ij}^{\ell}$ leads to

$$\mathbf{y}_{\ell} = \mathbf{H}_{\ell}\mathbf{f} + \boldsymbol{\omega} \tag{2.2}$$

where $\mathbf{y}_{\ell} \in \mathbb{R}^{V}$ is a vector representation of $\mathbf{Y}_{ij}^{\ell}$ with $V = N(N + L - 1)$,
$\mathbf{f} = \text{vec}([\mathbf{f}_0, ..., \mathbf{f}_{L-1}])$ is the vector representation of the data cube $\boldsymbol{\mathcal{F}}$, $\mathbf{f}_k$ is the vectorization of the k-th spectral band, and $\mathbf{H}_{\ell} \in \mathbb{R}^{V \times N^2 L}$ is the sensing matrix of the ℓ^{th} snapshot. The set of measurements associated with the K snapshots can be written as

$$\mathbf{y} = \mathbf{H}\mathbf{f} + \boldsymbol{\omega} \tag{2.3}$$

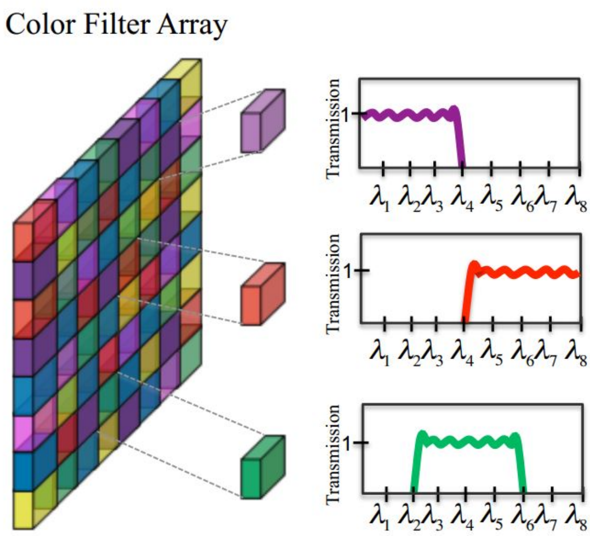

Figure 2.1: Colored coded aperture. Each pixel on the coded aperture is an optical filter whose spectral response can be selected. Source [43].

where $\mathbf{y} = [\mathbf{y}_0^T, ..., \mathbf{y}_{K-1}^T]^T$ contains all the measurements and $\mathbf{H} = [\mathbf{H}_0^T, ..., \mathbf{H}_{K-1}^T]^T \in \mathbb{R}^{KV \times N^2 L}$. An example of matrix $\mathbf{H}$ for $L = 3$ and $K = 2$ is displayed in Fig. 2.3. Note that the non-zero entries (indicated by white squares) of this matrix are determined by the 3D coded aperture. More precisely, the structure of the matrix $\mathbf{H}_\ell$ consists of a set of diagonal patterns determined by the ℓ^{th} colored coded aperture $\mathbf{T}^\ell$, which are located along the horizontal direction, such that one spatial dimension is shifted downward, as many times as the number of spectral bands. Finally, note that the structure of the complete matrix $\mathbf{H}$ is obtained by stacking the K matrices $\mathbf{H}_\ell$ for $\ell = 0, ..., K-1$.

2.2.2 Spatio-Spectral Coded Compressive Spectral Imager SSCSI.

Similar to colored-CASSI, SSCSI optically modulates the 3D data cube in both spatial and spectral dimensions, and acquires 2D projections. The SSCSI proposed in [26] uses a

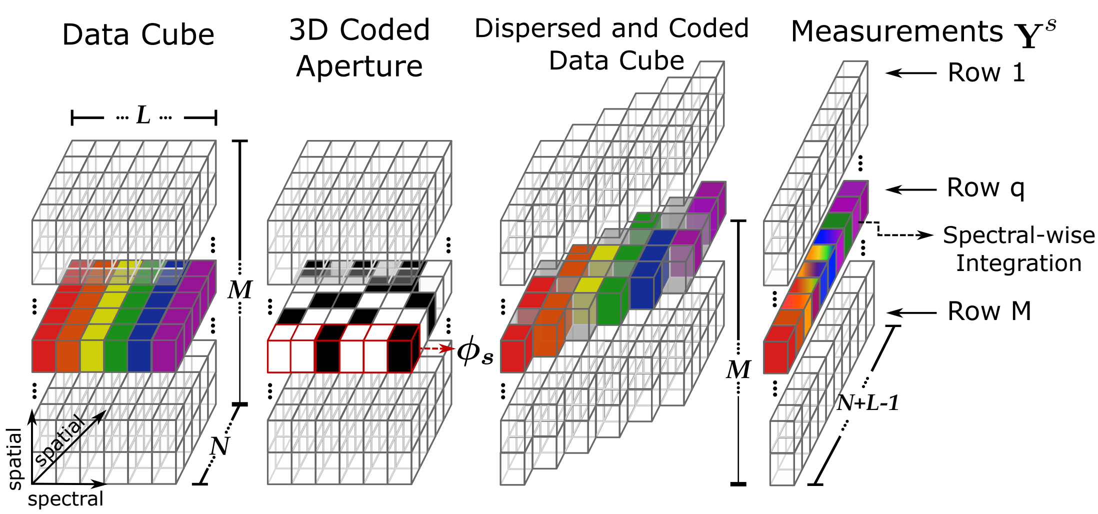

Figure 2.2: Schematic representation of the sensing phenomena behind CASSI system.

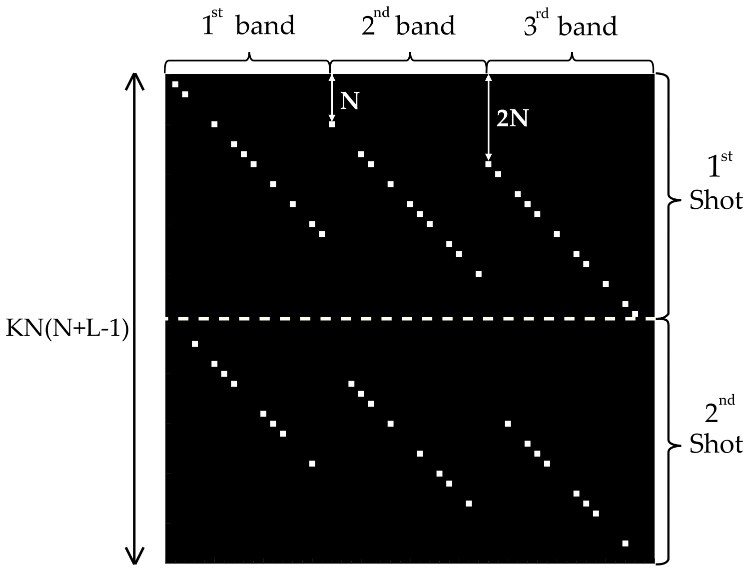

Figure 2.3: The sensing matrix $\mathbf{H}$ of the CASSI architecture for $L = 3$ and $K = 2$. The white squares represent the passing (non-blocking) elements.

diffraction grating to disperse the light into the spectrum plane and inserts a coding mask between the spectrum plane and the sensor plane to achieve the desired spatial-spectral modulation. A schematic representation of the compression procedure behind SSCSI is shown in Fig 2.4. The ℓ-th intensity at the (i, j)-th pixel of the SSCSI detector is defined as

$$Y_{ij}^{\ell} = \sum_{k=0}^{L-1} \mathcal{F}_{ijk} T_{ijk}^{\ell} + \omega_{ij}. \tag{2.4}$$

Note that SSCSI measurements are also defined as in (2.2) and (2.3) with $V = N^2$. However, the structure of the matrix $\mathbf{H}$ slightly differs from the one used in C-CASSI. It is also structured as a set of diagonal patterns but is not shifted downward. Moreover, the patterns do not repeat horizontally, allowing spectral coding. Fig 2.5 shows an example of matrix $\mathbf{H}$ associated with the SSCSI system.

2.3 Linear Mixing Model

The basic assumption in the linear mixing model (LMM) is that given a scene, the surface is constituted by a small number of distinct materials that have relatively constant spectral properties [30]. Thus, based on the LMM, it is assumed that each pixel of the hyperspectral image is a linear mixture of spectral signatures (referred to as endmembers) that represent each different substance. Hence, the mathematical model for an observed pixel $\mathbf{f}_j \in \mathbb{R}^L$ can be represented as $\mathbf{f}_j = \mathbf{M}\alpha_j$, where $\mathbf{M} \in \mathbb{R}^{L\times p}$ is the endmember matrix whose columns are spectral signatures, p is the number of materials contained in the image and $\alpha_j = [\alpha_{j1}, ..., \alpha_{jp}]^T \in \mathbb{R}^p$ represents the abundance fractions of the endmembers. Furthermore, using the LMM to represent every pixel in the image, we can describe a hyperspectral image as $\mathbf{f} = \overline{\mathbf{M}}\alpha$, where $\overline{\mathbf{M}} = \mathbf{M} \otimes \mathbf{I}$, $\mathbf{I} \in \mathbb{R}^{N^2\times N^2}$ is the identity matrix, $\otimes$ is the Kronecker product operation, and $\alpha = [\alpha_1^T, ..., \alpha_p^T]^T \in \mathbb{R}^{N^2 p}$, where $\alpha_k \in \mathbb{R}^{N^2}$ is the abundance

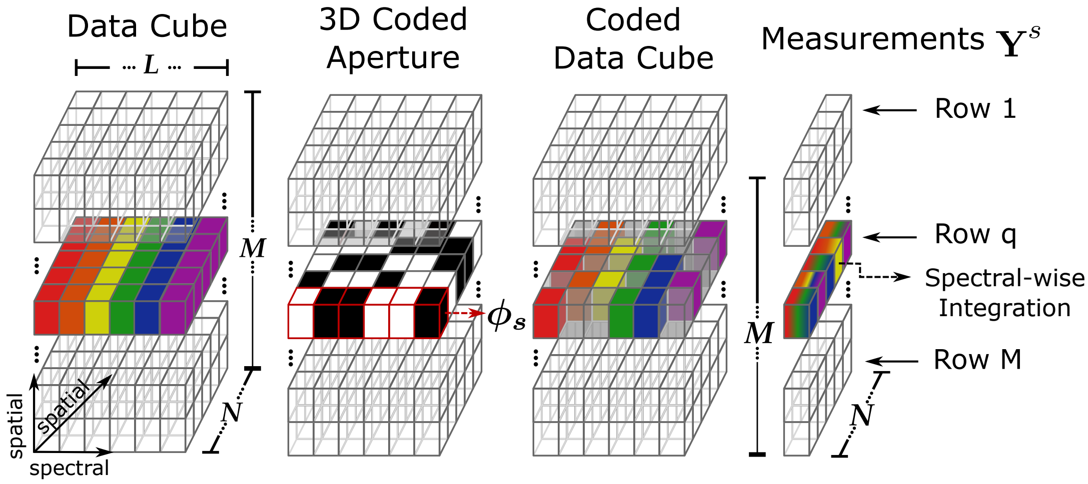

Figure 2.4: Schematic representation of the sensing phenomena behind SSCSI system.

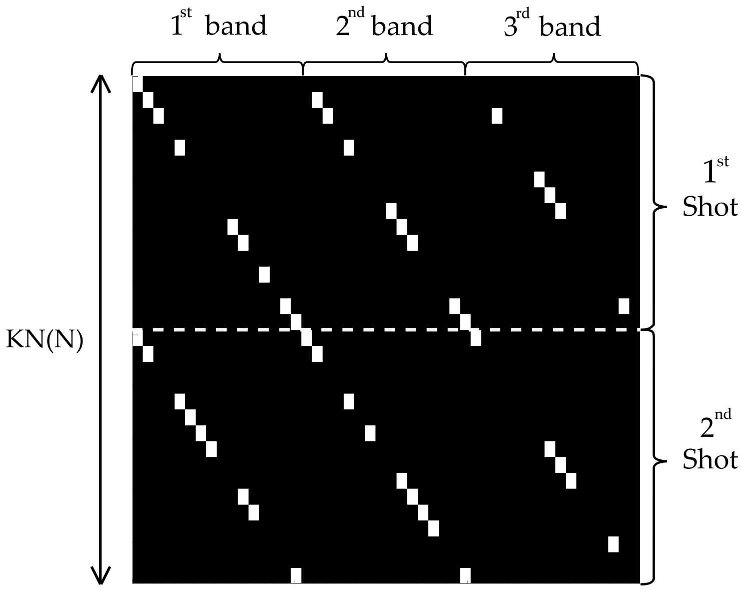

Figure 2.5: Example of sensing matrix $\mathbf{H}$ in the SSCSI architecture for $L = 3$ and $K = 1$. White squares are used for ones (unblocking light).

map of the k-th endmember, it accounts for the abundance of all pixels. At this point, it is important to mention that standard endmember extraction algorithms exist, such as VCA [31], SVMAX [32] or N-FINDR [33]. Unfortunately, the aforementioned unmixing algorithms cannot be used directly when the observed images have been compressed.

2.4 Hyperspectral and Multispectral Data Fusion

In all the traditional methods for HS data acquisition, due to technological reasons, there is a trade off between spectral and spatial resolution. Generally, HS images benefit from excellent spectroscopic properties with several or hundreds of thousands of contiguous bands but are limited by their relatively low spatial resolution [5]. Spaceborne imaging spectrometers are usually designed to provided data with a moderate ground sampling distance (GSD) [e.g.; 30 m]. To overcome the spatial resolution limitation, a common trend is to fuse images with different spectral and spatial resolutions. A typical example studied in this work is the fusion of HS images (having high spectral resolution) with multispectral (MS) images (having high spatial resolution) [16, 17]. Another example is HS pansharpening, which addresses the fusion of panchromatic and HS images [18]. Based on different theories such as component substitution, multiresolution analysis (MRA), spectral unmixing, and Bayesian probability, several HS-MS data fusion techniques have been proposed. See [44] for a comparative review of recent fusion algorithms. In this research work, we focus on fusion of HS and MS data based on the LMM. Unmixing based fusion aims at obtaining endmember information and high-resolution abundance matrices from the HS and MS images, respectively [20, 21]. To name a few, Yokoya et al. proposed Coupled Nonnegative Matrix Factorization (CNMF) [22], where the HS and MS data are alternately unmixed by NMF under the constraint of sensor observation models. In [21], Qi wei et al. proposed a fusion approach where a joint fusion and unmixing problem is formulated as maximizing the joint posterior distribution with respect to the endmember signatures and abundance problems. The common point of these works is to obtain endmembers from the HS image and abundance maps from the MS image alternatively.

2.5 Vertex Component Analysis

Vertex component analysis (VCA) is a numerical tool to estimate the endmembers of a scene under a linear mixing scenario, which exploits two facts: the endmembers are located at the vertices of a simplex and the affine transformation of a simplex is also a simplex [31]. Specifically, VCA models the spectral measurements as $\mathbf{y} = \mathbf{M}\gamma\boldsymbol{\alpha}$, where γ is a scale factor modeling the illumination variability, and the fractional abundance $\boldsymbol{\alpha}_j$ represents the fractional area occupied by the $\mathbf{m}_j$ endmember. This model leads to two constraints: the spectral signature is a nonnegative linear combination of endmemembers where the abundances sum to one. Thus the complete set of measurements $C_p = \{\mathbf{y} \in \mathbb{R}^L : \mathbf{y} = \mathbf{M}\gamma\boldsymbol{\alpha}, \boldsymbol{\alpha} \succeq 0, 1^T\boldsymbol{\alpha} = 1, \gamma \geq 0\}$ is a convex cone in $\mathbb{R}^L$. Based on this model, the VCA algorithm projects this cone onto a properly chosen hyperplane resulting in a simplex S_p with vertices being the endmembers. To find the endmembers, the algorithm works as follows (see [45][31] for more details):

1. Generate a random vector $\mathbf{f}$ orthonormal to the subspace spanned by the endmembers already determined.
2. Project the data $\mathbf{Y} = [\mathbf{y}_1, \cdots, \mathbf{y}_N]$, with N as the number of pixels, onto $\mathbf{f}$, i.e. $\mathbf{v} = \mathbf{Y}^T\mathbf{f}$.
3. Find the endmember $\mathbf{y}_k$ that maximizes the projection, where $k := \arg\max_{j=1,\cdots,N} |\mathbf{v}|$.
4. Repeat until all endmembers are exhausted.

2.6 Rayleigh-Ritz procedure

The Rayleigh-Ritz procedure is a method for finding approximations to eigenvalues and eigenvectors of a given matrix $\mathbf{A} \in \mathbb{R}^{n\times n}$ that cannot be solved analytically [46]. The procedure is as follows

1. Compute an orthonormal basis $\mathbf{B} \in \mathbb{R}^{n\times m}$, with $m \leq n$, approximating the eigenspace corresponding to m eigenvectors.

2. Compute $\mathbf{R} = \mathbf{B}^T\mathbf{AB}$.

3. Compute the eigenvalues of $\mathbf{R}$ solving $\mathbf{Rr}_i = \tilde{\lambda}_i\mathbf{r}_i$.

4. Form the Ritz pairs $(\tilde{\lambda}_i, \mathbf{u}_i) = (\tilde{\lambda}_i, \mathbf{Rr}_i)$, $i = 1, \cdots, m$.

Estimated Ritz pairs are the best approximations to the pairs $(\lambda_i, \mathbf{w}_i)$ for $i = 1, \cdots, m$, where λ_i and $\mathbf{w}_i$ are the eigenvalues and eigenvectors of the matrix $\mathbf{A}$, respectively. Further, the following theorem establishes how close are the m calculated Ritz pairs to $(\lambda_i, \mathbf{w}_i)$ for $i = 1, \cdots, m$.

Theorem 2.6.1. *Consider that the matrix* $\mathbf{A}$ *has spectrum* $\mathcal{S}_{\mathbf{A}} = \{\lambda_1(\mathbf{A}), \cdots, \lambda_N(\mathbf{A})\}$, *where the eigenvalues satisfy* $\lambda_1(\mathbf{A}) \geq \lambda_2(\mathbf{A}) \geq \cdots \geq \lambda_N(\mathbf{A})$. *The corresponding unit eigenvectors are* $\mathbf{w}_i$, *for all* $i = 1, \cdots, N$. *Suppose that, for a given Ritz vector* $\mathbf{u}_{k_0}$ *the eigenpair* $(\lambda_{k_0}(\mathbf{A}), \mathbf{w}_{k_0})$ *satisfies that*

$$\lambda_{k_0}(\mathbf{A}) = \arg\min_{\lambda \in \mathcal{S}_{\mathbf{A}}} |\lambda - \rho(\mathbf{u}_{k_0})|, \tag{2.5}$$

where $\rho(\mathbf{u_k}) = \mathbf{u}_k^T\mathbf{Au}_k$. *Then,*

$$|\sin(\phi_{k_0})| \leq \frac{\|\mathbf{Au}_{k_0} - \mathbf{u}_{k_0}\rho(\mathbf{u}_{k_0})\|_2}{\gamma_{k_0}}, \tag{2.6}$$

where ϕ_{k_0} *is the angle between* $\mathbf{u}_{k_0}$ *and* $\mathbf{w}_{k_0}$, *with*

$$\gamma_{k_0} = \min_{\lambda \in \mathcal{S}_{\mathbf{A}}, \lambda \neq \lambda_{k_0}(\mathbf{A})} |\lambda - \rho(\mathbf{u}_{k_0})|. \tag{2.7}$$

Proof. The proof of this theorem can be found in [46]. □

Notice that, from Theorem 2.6.1, the Ritz pairs $(\tilde{\lambda}_i, \mathbf{u}_i)$ can be considered a reasonable approximation to m eigenpairs $(\lambda_i(\mathbf{A}), \mathbf{w}_i)$, as it can be seen in (2.6).

3

Compressive Spectral Image Fusion

3.1 Problem statement

This section formulates the data fusion problem considered in this work to estimate a high-spatial high-spectral resolution image from two compressed images with different spectral and spatial resolutions.

3.1.1 Observation models. It is very common to assume that HS and MS images result from the application of linear spatial and linear spectral degradations to a higher resolution image $\mathbf{f} = \overline{\mathbf{M}}\boldsymbol{\alpha}$ [21, 47, 17]. Moreover, as we mentioned before, we propose to consider compressed spectral images that are modeled from linear projections. Thus we consider the following models for the observed compressed MS and HS images

$$\begin{aligned} \mathbf{y}_m = &\quad \mathbf{H}_m\mathbf{R}_\lambda\mathbf{f} + \mathbf{N}_m &= \mathbf{H}_m\mathbf{R}_\lambda\overline{\mathbf{M}}\boldsymbol{\alpha} + \mathbf{N}_m \\ \mathbf{y}_h = &\quad \mathbf{H}_h\mathbf{S}_\mathbf{s}\mathbf{f} + \mathbf{N}_h &= \mathbf{H}_h\mathbf{S}_\mathbf{s}\overline{\mathbf{M}}\boldsymbol{\alpha} + \mathbf{N}_h \end{aligned} \tag{3.1}$$

where

- $\mathbf{R}_\lambda = \mathbf{R}\otimes\mathbf{I}_{N^2}$ models the linear spectral degradation, and $\mathbf{R} \in \mathbb{R}^{L_m \times L}$ is the spectral response of the MS sensor.
- $\mathbf{S}_\mathbf{s} = \mathbf{I}_L \otimes \mathbf{SB}$ models the spatial degradation, $\mathbf{B} \in \mathbb{R}^{N^2 \times N^2}$ is a cyclic convolution operator acting on the bands, and $\mathbf{S} \in \mathbb{R}^{N_h^2 \times N^2}$ is a downsampling operator (satisfying the condition $\mathbf{S}\mathbf{S}^T = \mathbf{I}_{N_h^2}$)
- $\mathbf{H}_m \in \mathbb{R}^{n_m \times N^2 L_m}$ and $\mathbf{H}_h \in \mathbb{R}^{n_h \times N_h^2 L}$ are the sensing matrices for the MS and HS images, with n_m and n_h the numbers of measurements used to sense the MS and HS images. A more detailed description of the structure of the sensing matrices will be presented in the following section.
- $\mathbf{N}_m \in \mathbb{R}^{n_m}, \mathbf{N}_h \in \mathbb{R}^{n_h}$ are additive noise terms.
- $\mathbf{y}_m \in \mathbb{R}^{n_m}$ and $\mathbf{y}_h \in \mathbb{R}^{n_h}$ are the observed MS and HS compressed images.

The image restoration problem considered in this work consists of estimating the high resolution (HR) image $\mathbf{f}$ from the observed compressed measurements $\mathbf{y}_m$ and $\mathbf{y}_h$.

3.1.2 Problem formulation. Based on the previous models (3.1), we propose to consider the following optimization problem in order to estimate the matrix $\mathbf{M}$ and the vector $\boldsymbol{\alpha}$ from the observed compressive images $\mathbf{y}_m$ and $\mathbf{y}_h$

$$\begin{aligned} \underset{\mathbf{M},\boldsymbol{\alpha}}{\operatorname{argmin}} \quad & c(\mathbf{M},\boldsymbol{\alpha}) = f(\mathbf{M},\boldsymbol{\alpha}) + \varphi(\boldsymbol{\alpha}) \\ \text{subject to (s.t.)} \quad & \boldsymbol{\alpha} \geq 0, \mathbf{1}_p^T \mathbf{A} = \mathbf{1}_{N^2}^T, 0 \leq \mathbf{M} \leq 1 \end{aligned} \tag{3.2}$$

where $\geq$ means "element-wise greater than", $\mathbf{1}_p^T$ is a $p \times 1$ vector with all ones and

$$f(\mathbf{M},\boldsymbol{\alpha}) = \frac{1}{2}\|\mathbf{y}_m - \mathbf{H}_m\ \mathbf{R}_\lambda \overline{\mathbf{M}}\boldsymbol{\alpha}\|_2^2 + \frac{1}{2}\|\mathbf{y}_h - \mathbf{H}_h \mathbf{S}_\mathbf{s} \overline{\mathbf{M}}\boldsymbol{\alpha}\|_2^2$$

includes two data fidelity terms related to the MS and HS images. Finally,

$$\varphi(\boldsymbol{\alpha}) = \lambda\|\mathbf{G}\boldsymbol{\alpha}\|_1 + \lambda_{\text{TV}}\|\mathbf{D}\boldsymbol{\alpha}\|_1 \tag{3.3}$$

is a regularization operator, where the first term enforces sparsity of abundance maps in a wavelet representation and the second one includes a form of total variation (TV) regularizer preserving sharp edges or object boundaries [48]. The construction of the dictionary $\mathbf{G}$ and the matrix $\mathbf{D}$ will be detailed in the section devoted to numerical experiments. Note that $\|\cdot\|_2$ and $\|\cdot\|_1$ are used for the l_2 and l_1 norms, and that λ and λ_{TV} are regularization parameters. Note also that the constraints for α in (3.2) are the abundance non-negativity constraint (ANC) and the abundance sum-to-one constraint (ASC), which are classically used in hyperspectral imaging [30]. Moreover, the constraint for the matrix $\mathbf{M}$ expresses the fact that each spectral signature represents the reflectances of different materials that belong to the interval $[0, 1]$.

3.2 Optimization Method

This section studies the optimization algorithm that is proposed to solve (3.2). Note that this problem is nonconvex with respect to $(\mathbf{M},\boldsymbol{\alpha})$ [49], making its solution challenging. The strategy investigated here is a block coordinate descent (BCD) approach, alternating optimizations with respect to the matrix $\mathbf{M}$ and the vector $\boldsymbol{\alpha}$ [49]. The two resulting optimization problems are convex and can thus be solved using the ADMM algorithm [50]. A sketch of the proposed strategy is detailed in Algorithm 1. The initialization of the algorithm and the optimization steps with respect to $\boldsymbol{\alpha}$ and $\mathbf{M}$ are detailed in the following sections.

Algorithm 1: Proposed compressive image fusion

Input : $\mathbf{y}_m$, $\mathbf{y}_h$, $\mathbf{R}, \mathbf{B}, \mathbf{S}, \mathbf{H}_m, \mathbf{H}_h$
Output: $\hat{\boldsymbol{\alpha}}$ and $\widehat{\mathbf{M}}$
1: $\mathbf{M}^{(0)} = \text{EE}(\mathbf{y}_h)$ `%Endmember Extraction`
2: **for** $i = 1$ to stopping rule **do**
3: $\quad \boldsymbol{\alpha}^{(t)} = \underset{\boldsymbol{\alpha}\in\mathcal{A}}{\operatorname{argmin}} f(\mathbf{M}^{(t-1)},\boldsymbol{\alpha}) + \varphi(\boldsymbol{\alpha})$ `% AL 2`
4: $\quad \mathbf{M}^{(t)} = \underset{\mathbf{M}\in\mathcal{M}}{\operatorname{argmin}} f(\mathbf{M},\boldsymbol{\alpha}^{(t)})$ `% AL 4`
5: **end for**

3.2.1 Initialization. The endmember matrix is initialized with a fast estimation approach based on the Rayleigh-Ritz (RR) theory which was developed within this research work [51]. The idea of this method is to estimate the signal subspace from the compressive measurements using the RR theory and to estimate the endmembers using the fact that the LMM constrains the endmembers to be located at the vertices of a simplex. More precisely, this approach first estimates a subset of eigenvectors to approximate the signal subspace via RR theory, and then searches the endmembers in the approximated subspace using the vertex component analysis (VCA) (see the Appendix A for more details).

3.2.2 Optimization with respect to the abundance matrix. The first step of the minimization problem (3.2) optimizes the cost function with respect to $\boldsymbol{\alpha}$ for a fixed $\mathbf{M}$ using the ADMM algorithm. An auxiliary variable is introduced to split the objective function and the constraints leading to the following problem

$$\begin{array}{ll} \underset{\boldsymbol{\alpha},\mathbf{v}_i}{\operatorname{argmin}} & \frac{1}{2}\|\mathbf{y}_m - \mathbf{H}_m\mathbf{R}_\lambda\mathbf{v}_1\|_2^2 + \frac{1}{2}\|\mathbf{y}_h - \mathbf{H}_h\mathbf{S}_d\mathbf{v}_3\|_2^2 \\ & +\lambda\|\mathbf{v}_5\|_1 + \lambda_{TV}\|\mathbf{v}_6\|_1 + i_{\mathcal{A}}(\mathbf{v}_7) \\ \text{subject to} & \begin{array}{ll} \mathbf{v}_1 = \overline{\mathbf{M}}\mathbf{v}_2 & \mathbf{v}_5 = \mathbf{G}\boldsymbol{\alpha} \\ \mathbf{v}_2 = \boldsymbol{\alpha} & \mathbf{v}_6 = \mathbf{D}\boldsymbol{\alpha} \\ \mathbf{v}_3 = \overline{\mathbf{M}}\mathbf{v}_4 & \mathbf{v}_7 = \boldsymbol{\alpha} \\ \mathbf{v}_4 = \mathbf{B}_s\boldsymbol{\alpha} & \end{array} \end{array} \tag{3.4}$$

where $i = 1, ..., 7$, $\mathbf{S}_d = \mathbf{I}_L \otimes \mathbf{S}$, $\mathbf{B}_s = \mathbf{I}_p \otimes \mathbf{B}$, and the function $i_{\mathcal{A}}$ is defined on the set $\mathcal{A} = \{\boldsymbol{\alpha}|\boldsymbol{\alpha} \geq 0\}$ by

$$i_{\mathcal{A}}(\boldsymbol{\alpha}) = \begin{cases} 0 & \text{if } \boldsymbol{\alpha} \in \mathcal{A} \\ \infty & \text{if } \boldsymbol{\alpha} \notin \mathcal{A}. \end{cases} \tag{3.5}$$

Note that the number of splitting variables could have been reduced, e.g., by eliminating $\mathbf{v}_2$. However, the main motivation for the proposed algorithm is that it separates the spatial and spectral operations leading to subproblems which are simpler to solve. For convenience, we introduce the following notations

$$\mathbf{v} = \begin{bmatrix} \mathbf{v}_1 \\ \mathbf{v}_2 \\ \mathbf{v}_3 \\ \mathbf{v}_4 \\ \mathbf{v}_5 \\ \mathbf{v}_6 \\ \mathbf{v}_7 \end{bmatrix}, \mathbf{C} = \begin{bmatrix} \mathbf{0} \\ \mathbf{I} \\ \mathbf{0} \\ \mathbf{B}_s \\ \mathbf{G} \\ \mathbf{D} \\ \mathbf{I} \end{bmatrix}, \mathbf{E} = \begin{bmatrix} \mathbf{I} & -\overline{\mathbf{M}} & \mathbf{0} & \mathbf{0} & \mathbf{0} & \mathbf{0} & \mathbf{0} \\ \mathbf{0} & \mathbf{I} & \mathbf{0} & \mathbf{0} & \mathbf{0} & \mathbf{0} & \mathbf{0} \\ \mathbf{0} & \mathbf{0} & \mathbf{I} & -\overline{\mathbf{M}} & \mathbf{0} & \mathbf{0} & \mathbf{0} \\ \mathbf{0} & \mathbf{0} & \mathbf{0} & \mathbf{I} & \mathbf{0} & \mathbf{0} & \mathbf{0} \\ \mathbf{0} & \mathbf{0} & \mathbf{0} & \mathbf{0} & \mathbf{I} & \mathbf{0} & \mathbf{0} \\ \mathbf{0} & \mathbf{0} & \mathbf{0} & \mathbf{0} & \mathbf{0} & \mathbf{I} & \mathbf{0} \\ \mathbf{0} & \mathbf{0} & \mathbf{0} & \mathbf{0} & \mathbf{0} & \mathbf{0} & \mathbf{I} \end{bmatrix}$$

and the cost function

$$\begin{array}{rl} h(\mathbf{v}) = & \frac{1}{2}\|\mathbf{y}_m - \mathbf{H}_m\mathbf{R}_\lambda\mathbf{v}_1\|_2^2 + \frac{1}{2}\|\mathbf{y}_h - \mathbf{H}_h\mathbf{S}_d\mathbf{v}_3\|_2^2 \\ & +\lambda\|\mathbf{v}_5\|_1 + \lambda_{TV}\|\mathbf{v}_6\|_1 + i_{\mathcal{A}}(\mathbf{v}_7) \end{array}$$

with $\mathbf{E}\mathbf{v} = \mathbf{C}\boldsymbol{\alpha}$. Using these notations, (3.4) reduces to

$$\begin{array}{rl} \underset{\boldsymbol{\alpha},\mathbf{v}}{\operatorname{argmin}} & h(\mathbf{v}) \\ \text{subject to} & \mathbf{E}\mathbf{v} = \mathbf{C}\boldsymbol{\alpha}. \end{array} \tag{3.6}$$

The augmented Lagrangian associated with (3.6) is

$$\mathcal{L}(\boldsymbol{\alpha}, \mathbf{v}, \mathbf{g}) = h(\mathbf{v}) + \frac{\rho}{2}\|\mathbf{E}\mathbf{v} - \mathbf{C}\boldsymbol{\alpha} + \mathbf{g}\|_2^2 \tag{3.7}$$

where $\mathbf{g}$ is the scaled dual variable and $\rho \geq 0$ is weighting the augmented Lagrangian term. The exact procedure used for estimating $\boldsymbol{\alpha}$ is summarized in Algorithm 2.

Algorithm 2: ADMM algorithm to estimate $\boldsymbol{\alpha}$

Input : $\mathbf{y}_m, \mathbf{y}_h, \mathbf{R}, \mathbf{B}, \mathbf{S}, \mathbf{H}_m, \mathbf{H}_h, \mathbf{M}, \rho \geq 0$
Output: $\boldsymbol{\alpha}^{(k+1)}$

$\mathbf{v}^{(0)}, \mathbf{g}^{(0)}$
for $k = 1$ to stopping rule **do**
  $\boldsymbol{\alpha}^{(k+1)} = \underset{\boldsymbol{\alpha}}{\operatorname{argmin}} \ \mathcal{L}(\boldsymbol{\alpha}, \mathbf{v}^{(k)}, \mathbf{g}^{(k)})$
  $\mathbf{v}^{(k+1)} = \underset{\mathbf{v}}{\operatorname{argmin}} \ \mathcal{L}(\boldsymbol{\alpha}^{(k+1)}, \mathbf{v}, \mathbf{g}^{(k)})$
  $\mathbf{g}^{(k+1)} = \mathbf{g}^{(k)} + \mathbf{v}^{(k+1)} - \mathbf{C}\boldsymbol{\alpha}^{(k+1)}$
end for

The augmented Lagrangian (3.7) associated with the optimization problem (3.6) can be rewritten, in detail, as

$$
\begin{aligned}
\mathcal{L}(\boldsymbol{\alpha}, \mathbf{v}, \mathbf{g}) &= \tfrac{1}{2}\|\mathbf{y}_m - \mathbf{H}_m\mathbf{R}_\lambda\mathbf{v}_1\|_2^2 + \tfrac{1}{2}\|\mathbf{y}_h - \mathbf{H}_h\mathbf{S}_d\mathbf{v}_3\|_2^2 \\
&+\lambda\|\mathbf{v}_5\|_1 + \lambda_{\mathrm{TV}}\|\mathbf{v}_6\|_1 + i_{\mathcal{A}}(\mathbf{v}_7) + \tfrac{\rho}{2}\|\mathbf{v}_1 - \overline{\mathbf{M}}\mathbf{v_2} + \mathbf{g_1}\|_2^2 \\
&+\tfrac{\rho}{2}\|\mathbf{v}_2 - \boldsymbol{\alpha} + \mathbf{g}_2\|_2^2 + \tfrac{\rho}{2}\|\mathbf{v}_3 - \overline{\mathbf{M}}\mathbf{v}_4 + \mathbf{g}_3\|_2^2 \\
&+\tfrac{\rho}{2}\|\mathbf{v}_4 - \mathbf{B}_s\boldsymbol{\alpha} + \mathbf{g}_4\|_2^2 + \tfrac{\rho}{2}\|\mathbf{v}_5 - \mathbf{G}\boldsymbol{\alpha} + \mathbf{g}_5\|_2^2 \\
&+\tfrac{\rho}{2}\|\mathbf{v}_6 - \mathbf{D}\boldsymbol{\alpha} + \mathbf{g}_6\|_2^2 + \tfrac{\rho}{2}\|\mathbf{v}_7 - \boldsymbol{\alpha} + \mathbf{g}_7\|_2^2.
\end{aligned}
\tag{3.8}
$$

Thus, the different detailed steps for the estimation of $\boldsymbol{\alpha}$ using the ADMM algorithm can be summarized in Algorithm 3 whereas more details are provided below.

Algorithm 3: ADMM algorithm to estimate $\boldsymbol{\alpha}$

Input : $\mathbf{y}_m, \mathbf{y}_h, \mathbf{R}, \mathbf{B}, \mathbf{S}, \mathbf{H}_m, \mathbf{H}_h, \mathbf{M}, \rho \geq 0$
Output: $\boldsymbol{\alpha}^{(k+1)}$

$\mathbf{v}^{(0)}, \mathbf{g}^{(0)}$
for $k = 1$ to stopping rule **do**
  $\boldsymbol{\alpha}^{(k+1)} = \underset{\boldsymbol{\alpha}}{\operatorname{argmin}} \ \mathcal{L}(\boldsymbol{\alpha}, \mathbf{v}_i^{(k)}, \mathbf{g}_i^{(k)})$
  for $l = 1$ to 7 **do**
    $\mathbf{v}_l^{(k+1)} = \underset{\mathbf{v}_l}{\operatorname{argmin}} \ \mathcal{L}(\boldsymbol{\alpha}^{(k+1)}, \mathbf{v}_l, \mathbf{v}_i, \mathbf{g}_i^{(k)})$
  end for
  $\mathbf{g}_1^{(k+1)} = \mathbf{g}_1^{(k)} + \mathbf{v}_1^{(k+1)} - \boldsymbol{\alpha}^{(k+1)}$
  $\mathbf{g}_2^{(k+1)} = \mathbf{g}_2^{(k)} + \mathbf{v}_2^{(k+1)} - \mathbf{B}_s\boldsymbol{\alpha}^{(k+1)}$
  $\mathbf{g}_3^{(k+1)} = \mathbf{g}_3^{(k)} + \mathbf{v}_3^{(k+1)} - \mathbf{G}\boldsymbol{\alpha}^{(k+1)}$
  $\mathbf{g}_4^{(k+1)} = \mathbf{g}_4^{(k)} + \mathbf{v}_4^{(k+1)} - \mathbf{D}\boldsymbol{\alpha}^{(k+1)}$
  $\mathbf{g}_5^{(k+1)} = \mathbf{g}_5^{(k)} + \mathbf{v}_5^{(k+1)} - \boldsymbol{\alpha}^{(k+1)}$
end for

Updating α. To find the solution $\boldsymbol{\alpha}$ of the first minimization problem, we force the derivative of (3.8) with respect to $\boldsymbol{\alpha}$ to be zero and solve the resultant system, leading to

$$\boldsymbol{\alpha} = \left(3\mathbf{I} + \mathbf{B}_s^T\mathbf{B}_s + \mathbf{D}^T\mathbf{D}\right)^{-1}\boldsymbol{\Xi} \tag{3.9}$$

where $\boldsymbol{\Xi} = \mathbf{v}_2 + \mathbf{g}_2 + \mathbf{B}_s^T(\mathbf{v}_4 + \mathbf{g}_4) + \mathbf{G}^T(\mathbf{v}_5 + \mathbf{g}_5) + \mathbf{D}^T(\mathbf{v}_6 + \mathbf{g}_6) + \mathbf{v}_7 + \mathbf{g}_7$.
Due to the circular structure of matrices $\mathbf{B}_s$ and $\mathbf{D}$, we can efficiently compute the solution using the fast Fourier transform, with a complexity of $\mathcal{O}(p \times N\log N)$.

Updating $\mathbf{v}_1$. The minimization problem involving $\mathbf{v}_1$ can be obtained by solving $\partial\mathcal{L}/\partial\mathbf{v}_1 = 0$, leading to

$$\mathbf{v}_1 = \left(\mathbf{E}^T\mathbf{E} + \rho\mathbf{I}\right)^{-1}\boldsymbol{\Theta} \tag{3.10}$$

where $\mathbf{E} = \mathbf{H}_m\mathbf{R}_\lambda$ and $\boldsymbol{\Theta} = \mathbf{E}^T\mathbf{y}_m + \overline{\mathbf{M}}\mathbf{v}_2 - \mathbf{g}_1$. Note that the inverse matrix in (3.10) can be precomputed. It should be noted that if we consider an MS image of size $256 \times 256 \times 10$ the size of matrix to be inverted is 655360×655360, which is high. To solve this problem efficiently we can take advantage of the structure of the sensing ($\mathbf{H}_m$) and downsampling ($\mathbf{R}_\lambda$) matrices to rearrange the matrix $\mathbf{E}$ in a block diagonal matrix $\tilde{\mathbf{E}}$ which is easier to invert. As explained in [52], it can be achieved using two unitary matrices $\mathbf{R}_1$ and $\mathbf{R}_2$ such that $\tilde{\mathbf{E}} = \mathbf{R}_2\mathbf{E}\mathbf{R}_1^T$ (for more details about the matrices $\mathbf{R}_1$ and $\mathbf{R}_2$, the reader is invited to consult [52]). Considering that we have K_m snapshots to acquire the MS image $\mathbf{f}_m$, this step has complexity $\mathcal{O}(K_mV)$, where V was defined in Section III. We did not encounter any numerical problem when using this strategy.

Updating $\mathbf{v}_2$. To minimize the Lagrangian (3.8) with respect to $\mathbf{v}_2$, we solve $\partial\mathcal{L}/\partial\mathbf{v}_2 = 0$, yielding

$$\mathbf{v}_2 = \left(\overline{\mathbf{M}}^T\overline{\mathbf{M}} + \mathbf{I}\right)^{-1}\boldsymbol{\Gamma} \tag{3.11}$$

where $\boldsymbol{\Gamma} = \overline{\mathbf{M}}^T(\mathbf{v}_1 + \mathbf{g}_1) + \boldsymbol{\alpha} - \mathbf{g}_2$. Since $\left(\overline{\mathbf{M}}^T\overline{\mathbf{M}} + \mathbf{I}\right)^{-1} = \left(\mathbf{M}^T\mathbf{M} + \mathbf{I}\right)^{-1} \otimes \mathbf{I}$, the inverse term in (3.11) can be easily computed by calculating the inverse of the matrix $\mathbf{M}^T\mathbf{M} + \mathbf{I} \in \mathbf{R}^{p\times p}$ which is of small size due to the small number the endmembers p contained in a scene. The complexity of this step is $\mathcal{O}(N^2p)$.

Updating $\mathbf{v}_3$. To update $\mathbf{v}_3$, we solve the equation $\partial\mathcal{L}/\partial\mathbf{v}_3 = 0$, whose solution is

$$\mathbf{v}_3 = \left(\mathbf{F}^T\mathbf{F} + \rho\mathbf{I}\right)^{-1}\boldsymbol{\Delta} \tag{3.12}$$

where $\mathbf{F} = \mathbf{H}_h\mathbf{S}_d$ and $\boldsymbol{\Delta} = \mathbf{F}^T\mathbf{y}_h + \overline{\mathbf{M}}\mathbf{v}_4 - \mathbf{g}_3$. Note also that the inverse matrix in (3.12) can be pre-computed. If we consider, e.g., an HS image of size $128 \times 128 \times 160$, we need to invert a huge matrix of size 2621440×2621440. This problem can be solved by rearranging the matrix $\mathbf{F}$ as for $\mathbf{E}$ in (3.10). If K_h snapshots have been used to acquire the HS image $\mathbf{f}_h$, the complexity of computing $\mathbf{v}_3$ is $\mathcal{O}(K_hV)$.

Updating $\mathbf{v}_4$. The update of $\mathbf{v}_4$ can be found by solving $\partial\mathcal{L}/\partial\mathbf{v}_4 = 0$, whose solution is

$$\mathbf{v}_4 = \left(\overline{\mathbf{M}}^T\overline{\mathbf{M}} + \mathbf{I}\right)^{-1}\boldsymbol{\Lambda} \tag{3.13}$$

where $\boldsymbol{\Lambda} = \overline{\mathbf{M}}^T(\mathbf{v}_3 + \mathbf{g}_3) + \mathbf{B}_s\boldsymbol{\alpha} - \mathbf{g}_4$. Note that the inverse term is the same as in (3.11). The complexity to update $\mathbf{v}_4$ is $\mathcal{O}(N^2p)$.

Updating $\mathbf{v}_5$. The minimization with respect to $\mathbf{v}_5$ corresponds to the scaled proximal operator of the closed, proper and convex function $\|\cdot\|_1$, i.e.,

$$\underset{\mathbf{v}_5}{\operatorname{argmin}} \ \lambda\|\mathbf{v}_5\|_1 + \frac{\rho}{2}\|\mathbf{v}_5 - \mathbf{G}\boldsymbol{\alpha} + \mathbf{g}_5\|_2^2 \tag{3.14}$$

whose solution is defined using the soft-thresholding operator

$$\mathbf{v}_5 = \mathcal{S}_{\lambda/\rho}\left(\mathbf{G}\boldsymbol{\alpha} - \mathbf{g}_5\right) \tag{3.15}$$

where $\mathcal{S}_\epsilon(\cdot)$ is the soft-thresholding function defined as $\mathcal{S}_\epsilon(\mathbf{s}) = \operatorname{sgn}(\mathbf{s}) \odot \max(0, |\mathbf{s}| - \epsilon)$. The complexity to obtain $\mathbf{v}_5$ is of the order $\mathcal{O}(p \times N\log N)$.

Updating $\mathbf{v}_6$. Similarly to the optimization with respect to $\mathbf{v}_5$, the minimization problem for $\mathbf{v}_6$ leads to

$$\mathbf{v}_6 = \mathcal{S}_{\lambda_{TV}/\rho}\left(\mathbf{D}\boldsymbol{\alpha} - \mathbf{g}_6\right). \tag{3.16}$$

The complexity of this step is also of the order $\mathcal{O}(p \times N\log N)$.

Updating $\mathbf{v}_7$. The minimization with respect to $\mathbf{v}_7$ is the proximal operator of the indicator function of the convex set $\mathcal{A}$ which reduces to Euclidean projection onto $\mathcal{A}$, i.e.,

$$\Pi_{\mathcal{A}}(\boldsymbol{\alpha} - \mathbf{g}_7) = \underset{\mathbf{v}_7 \in \mathcal{A}}{\operatorname{argmin}} \ \|\mathbf{v}_7 - (\boldsymbol{\alpha} - \mathbf{g}_7)\|_2^2. \tag{3.17}$$

The total complexity of the Algorithm 3 is dominated by the update steps of $\mathbf{v}_1$ and $\mathbf{v}_3$ being $\mathcal{O}(K_h N_h(N_h + L - 1) + K_m N(N + L_m - 1))$ for the C-CASSI system and $\mathcal{O}(K_h N_h^2 + K_m N^2)$ for the SSCSI system.

Convergence. In order to guarantee the convergence of Algorithm 2, we need to ensure that the augmented Lagrangian in (3.7) is a proper convex and closed function, according to the ADMM algorithm. This condition is satisfied since (3.7) is the sum of nonnegative convex functions [50]. Moreover, since the proper convex optimization function is continuous, it is closed, ensuring the convergence of Algorithm 2 [53].

3.2.3 Optimization with respect to the endmember matrix.

The optimization of the cost function (3.2) with respect to $\mathbf{M}$ for a fixed $\boldsymbol{\alpha}$ can be solved by using the ADMM algorithm. To facilitate the solution of this problem, we first rewrite the HS image as $\mathbf{f} = \overline{\mathbf{A}}\mathbf{m}$, where $\mathbf{m} = \operatorname{vec}(\mathbf{M}^T)$, $\overline{\mathbf{A}} = \mathbf{I}_L \otimes \mathbf{A}^T$, and $\mathbf{A} = [\boldsymbol{\alpha}_1, ..., \boldsymbol{\alpha}_{N^2}]$ contains the abundances of all the image pixels. This reparameterization leads to

$$\begin{aligned} \underset{\mathbf{m}}{\operatorname{argmin}} \quad & \tfrac{1}{2}\|\mathbf{y}_m - \mathbf{H}_m\mathbf{R}_\lambda\overline{\mathbf{A}}\mathbf{m}\|_2^2 + \tfrac{1}{2}\|\mathbf{y}_h - \mathbf{H}_h\mathbf{S}_\mathbf{s}\overline{\mathbf{A}}\mathbf{m}\|_2^2 \\ & + i_{\mathcal{M}}(\mathbf{m}) \end{aligned} \tag{3.18}$$

where the function $i_{\mathcal{M}}(\mathbf{m})$ is a function defined in the set $\mathcal{M} = \{\mathbf{m}|0 \leq \mathbf{m} \leq 1\}$ as in (3.5). To solve this problem, we split the vector $\mathbf{m}$ into three auxiliary variables $\mathbf{w}_1$, $\mathbf{w}_2$, $\mathbf{w}_3$ in order to obtain the following problem

$$\begin{aligned} \underset{\mathbf{m}, \mathbf{w}_i}{\operatorname{argmin}} \quad & \tfrac{1}{2}\|\mathbf{y}_m - \mathbf{H}_m\mathbf{R}_\lambda\mathbf{w}_1\|_2^2 + \tfrac{1}{2}\|\mathbf{y}_h - \mathbf{H}_h\mathbf{S}_d\mathbf{w}_2\|_2^2 \\ & + i_{\mathcal{M}}(\mathbf{w}_3) \\ \text{subject to} \quad & \mathbf{w}_1 = \overline{\mathbf{A}}\mathbf{m} \qquad \mathbf{w}_3 = \mathbf{m} \\ & \mathbf{w}_2 = \widehat{\mathbf{A}}\mathbf{m} \end{aligned} \tag{3.19}$$

where $j = 1, ..., 3$, and $\widehat{\mathbf{A}} = \mathbf{I}_L \otimes \mathbf{BA}$. For notational convenience, we introduce the following quantities

$$\mathbf{w} = \begin{bmatrix} \mathbf{w}_1 \\ \mathbf{w}_2 \\ \mathbf{w}_3 \end{bmatrix}, \mathbf{E} = \begin{bmatrix} \overline{\mathbf{A}} \\ \widehat{\mathbf{A}} \\ \mathbf{I} \end{bmatrix}$$

and the cost function

$$l(\mathbf{w}) = \frac{1}{2}\|\mathbf{y}_m - \mathbf{H}_m \mathbf{R}_\lambda \mathbf{w}_1\|_2^2 + \frac{1}{2}\|\mathbf{y}_h - \mathbf{H}_h \mathbf{S}_d \mathbf{w}_2\|_2^2 + g(\mathbf{w}_3).$$

As a consequence, the problem (3.19) reduces to

$$\begin{array}{ll} \underset{\mathbf{m},\mathbf{w}}{\operatorname{argmin}} & l(\mathbf{w}) \\ \text{subject to} & \mathbf{w} = \mathbf{Em} \end{array} \tag{3.20}$$

with the following augmented Lagrangian

$$\mathcal{L}(\mathbf{m}, \mathbf{w}, \mathbf{d}) = l(\mathbf{w}) + \tfrac{\rho}{2}\|\mathbf{w} - \mathbf{Em} + \mathbf{d}\|_2^2 \tag{3.21}$$

where $\mathbf{d}$ is the scaled dual variables and $\rho \geq 0$ is weighting the augmented Lagrangian term. The ADMM algorithm for $\mathbf{m}$ is summarized in Algorithm 4.

Algorithm 4: ADMM algorithm to estimate $\mathbf{m}$

Input : $\mathbf{y}_m$,$\mathbf{y}_h$,$\mathbf{R}, \mathbf{B}, \mathbf{S}, \mathbf{H}_m, \mathbf{H}_h, \boldsymbol{\alpha}, \rho \geq 0$

Output: $\mathbf{m}^{(k+1)}$

1: $\mathbf{w}^{(0)}, \mathbf{d}^{(0)}$

2: **for** $k = 1$ to stopping rule **do**

3: $\quad \mathbf{m}^{(k+1)} = \underset{\mathbf{m}}{\operatorname{argmin}}\ \mathcal{L}(\mathbf{m}, \mathbf{w}^{(k)}, \mathbf{d}^{(k)})$

4: $\quad \mathbf{w}^{(k+1)} = \underset{\mathbf{w}}{\operatorname{argmin}}\ \mathcal{L}(\mathbf{m}^{(k+1)}, \mathbf{w}, \mathbf{d}^{(k)})$

5: $\quad \mathbf{d}^{(k+1)} = \mathbf{d}^{(k)} + \mathbf{w}^{(k+1)} - \mathbf{Em}^{(k+1)}$

6: **end for**

Similar to the previous algorithm, we define the augmented Lagrangian (3.21), in detail, associated with the problem (3.19), i.e.,

$$\begin{aligned} &\mathcal{L}(\boldsymbol{\alpha}, \mathbf{w}, \mathbf{d}) = \tfrac{1}{2}\|\mathbf{y}_m - \mathbf{H}_m \mathbf{R}_\lambda \mathbf{w}_1\|_2^2 + \tfrac{1}{2}\|\mathbf{y}_h - \mathbf{H}_h \mathbf{S}_d \mathbf{w}_2\|_2^2 \\ &+ i_{\mathcal{M}}(\mathbf{w}_3) + \tfrac{\rho}{2}\|\mathbf{w}_1 - \overline{\mathbf{A}}\mathbf{m} + \mathbf{d}_1\|_2^2 + \tfrac{\rho}{2}\|\mathbf{w}_2 - \widehat{\mathbf{A}}\mathbf{m} + \mathbf{d}_2\|_2^2 \\ &+ \tfrac{\rho}{2}\|\mathbf{w}_3 - \mathbf{m} + \mathbf{d}_3\|_2^2. \end{aligned} \tag{3.22}$$

Based on this Lagrangian, the different steps of the ADMM algorithm are summarized in Algorithm 5. More details are provided below.

Updating m. To update $\mathbf{m}$, we solve the equation $\partial \mathcal{L} / \partial \mathbf{m} = 0$ whose solution is

$$\mathbf{m} = \left(\mathbf{I} + \overline{\mathbf{A}}^T \overline{\mathbf{A}} + \widehat{\mathbf{A}}^T \widehat{\mathbf{A}} \right)^{-1} \xi \tag{3.23}$$

where $\xi = \overline{\mathbf{A}}^T(\mathbf{w}_1 + \mathbf{d}_1) + \widehat{\mathbf{A}}^T(\mathbf{w}_2 + \mathbf{d}_2) + \mathbf{w}_3 + \mathbf{d}_3$. Note that the inverse matrix appearing in the right hand side can be pre-computed before the iterations. Computing the expression of $\mathbf{m}$ has a complexity of the order $\mathcal{O}(p \times N^2)$.

Algorithm 5: ADMM algorithm to estimate $\boldsymbol{\alpha}$

Input : $\mathbf{y}_m$,$\mathbf{y}_h$,$\mathbf{R}, \mathbf{B}, \mathbf{S}, \mathbf{H}_m, \mathbf{H}_h, \mathbf{M}, \rho \geq 0$

Output: $\boldsymbol{\alpha}^{(k+1)}$

1: $\mathbf{v}^{(0)}, \mathbf{d}^{(0)}$

2: **for** $k = 1$ to stopping rule **do**

3: $\quad \mathbf{m}^{(k+1)} = \underset{\mathbf{m}}{\text{argmin}} \;\; \mathcal{L}(\boldsymbol{\alpha}, \mathbf{w}_i^{(k)}, \mathbf{d}_i^{(k)})$

4: $\quad$ **for** $l = 1$ to 3 **do**

5: $\quad\quad \mathbf{w}_l^{(k+1)} = \underset{\mathbf{w}_l}{\text{argmin}} \;\; \mathcal{L}(\mathbf{m}^{(k+1)}, \mathbf{w}_l, \mathbf{w}_i, \mathbf{d}_i^{(k)})$

6: $\quad$ **end for**

7: $\quad \mathbf{d}_1^{(k+1)} = \mathbf{d}_1^{(k)} + \mathbf{w}_1^{(k+1)} - \overline{\mathbf{A}}\mathbf{m}^{(k+1)}$

8: $\quad \mathbf{d}_2^{(k+1)} = \mathbf{d}_2^{(k)} + \mathbf{w}_2^{(k+1)} - \widehat{\mathbf{A}}\mathbf{m}^{(k+1)}$

9: $\quad \mathbf{d}_3^{(k+1)} = \mathbf{d}_3^{(k)} + \mathbf{w}_3^{(k+1)} - \mathbf{m}^{(k+1)}$

10: **end for**

Updating $\mathbf{w}_1$. The minimization of (3.22) with respect to $\mathbf{w}_1$ can be obtained by solving $\partial\mathcal{L}/\partial\mathbf{w}_1 = 0$, leading to

$$\mathbf{w}_1 = \left(\mathbf{E}^T\mathbf{E} + \rho\mathbf{I}\right)^{-1}\boldsymbol{\Theta} \tag{3.24}$$

where $\mathbf{E} = \mathbf{H}_m\mathbf{R}_\lambda$ and $\boldsymbol{\Theta} = \mathbf{E}^T\mathbf{y}_m + \overline{\mathbf{A}}\mathbf{m} - \mathbf{d}_1$. Again, the inverse matrix is the same as in (3.10) and can be precomputed.

Updating $\mathbf{w}_2$. To minimize the Lagrangian (3.22) with respect to $\mathbf{v}_2$, we solve $\partial\mathcal{L}/\partial\mathbf{v}_2 = 0$, yielding

$$\mathbf{w}_2 = \left(\mathbf{F}^T\mathbf{F} + \rho\mathbf{I}\right)^{-1}\boldsymbol{\Delta} \tag{3.25}$$

where $\mathbf{F} = \mathbf{H}_h\mathbf{S}_d$ and $\boldsymbol{\Delta} = \mathbf{F}^T\mathbf{y}_h + \widehat{\mathbf{A}}\mathbf{m} - \mathbf{d}_2$. Note that the inverse term is the same as in (3.12) and can be computed efficiently.

Updating $\mathbf{w}_3$. Minimizing the Lagrangian with respect to $\mathbf{w}_3$ involves the proximal operator of the indicator function of the set $\mathcal{M}$, whose solution is obtained by computing the Euclidean projection of $\mathbf{m} - \mathbf{g}_3$ onto the convex set $\mathcal{M}$. i.e.,

$$\Pi_{\mathcal{M}}(\mathbf{m} - \mathbf{g}_3) = \underset{\mathbf{w}_3 \in \mathcal{M}}{\text{argmin}} \;\; \|\mathbf{w}_3 - (\mathbf{m} - \mathbf{g}_3)\|_2^2. \tag{3.26}$$

The complexity of Algorithm 5 is dominated by the update steps of $\mathbf{w}_1$ and $\mathbf{w}_2$ being $\mathcal{O}(K_hN_h(N_h+L-1)+K_mN(N+L_m-1))$ for the C-CASSI system and $\mathcal{O}(K_hN_h^2+K_mN^2)$ for the SSCSI system.

Convergence. The energy function (3.21) is proper convex since it corresponds to the sum of nonnegative convex functions. Moreover, since the proper convex optimization function is continuous, it is closed guaranteeing the convergence of Algorithm 3 [53].

3.2.4 Global algorithm convergence.

Given that the optimization problem in (3.2) viewed as a function of $\boldsymbol{\alpha}$ or $\mathbf{M}$ separately is convex and attains a unique minimum, from Theorem 4.1 in [54], we know that every limit point of the sequence $\{\boldsymbol{\alpha}^{(t)}, \mathbf{M}^{(t)}\}$ generated by Algorithm 1 is a stationary point of the considered optimization problem.

4

Simulation Results

4.1 Simulation Results

This section studies fusion results for HS and MS compressed images obtained using the proposed algorithm for three different datasets with available ground truth. Following Wald's protocol [18], each reference image was degraded to generate the MS and HS images to be fused. The HS image was generated by applying a spatial blur to the reference image with a 7×7 Gaussian filter with standard deviation $\sigma = 1.5$ and by downsampling the result by a factor of 4 in each direction. The MS image was generated by uniformly downsampling the spectral dimension of the reference image resulting in an M-band MS image, with $\mathrm{M} \in \{6, 9, 10\}$, for datasets 1, 2, and 3, respectively. The observed HS and MS images were finally compressed using C-CASSI or SSCSI systems with sensing matrices whose entries were generated using a Bernoulli distribution. Indeed, the optical filters can be modeled as realizations of a Bernoulli random variable where the value "1" corresponds to a light transmissive element and the value "0" to a blocking element [27, 25]. The compression ratio was fixed to 0.5. Additionally, the HS and MS compressed images were both contaminated by additive white Gaussian noise, with a signal to noise ratio equal to $\mathrm{SNR} = 30$ dB for every snapshot.
Before running the proposed algorithm, we need to define the matrices $\mathbf{G}$, $\mathbf{D}$ and the different hyperparameters in (3.3). Following [25], the dictionary $\mathbf{G}$ was selected as the Kronecker product $\mathbf{I}_p \otimes \boldsymbol{\Psi}$, where $\boldsymbol{\Psi}$ is a Symlet wavelet kernel. The operator $\mathbf{D}$ was decoupled in two operators acting on the rows and columns of each abundance map, as explained in [55]. Tuning the regularization hyperparameters is an interesting and complex problem. However, experimentally we noted that constant values for these parameters provided very interesting results. Thus, the hyperparameters λ, λ_{TV} and ρ were fixed for all datasets and were determined by cross-validation leading to $\lambda = \lambda_{TV} = 0.006$ and $\rho = 0.005$ for C-CASSI and $\lambda = \lambda_{TV} = 0.001$ and $\rho = 0.001$ for SSCSI.
The results obtained with the proposed fusion strategy are compared with the FUMI method of [21] (that does not use compressive measurements) and with the compressive fusion strategy proposed in [23] (that does not use spectral unmixing). We also consider the method studied in [24] for the first dataset (Jasper)[1]. Since the approach in [24] processes images with the same spatial and spectral resolutions, we upsampled the HS image to the

[1]The authors are very grateful to T. Wan and A. Achim for sharing their codes allowing a fair comparison.

spatial resolution of the MS image and the MS image to the spectral resolution of the MS image by bicubic interpolation. The approach of [24] was then applied band per band to the two interpolated images.

4.1.1 Jasper dataset. The Jasper ridge HS image is of size $128 \times 128 \times 66$ [56] [57] and contains $p = 4$ endmembers. Quantitative fusion results are reported in Table 4.1 whereas qualitative fusion results are displayed in Figs. 4.1 and 4.2. The reconstructed images using the proposed algorithm are displayed in Figs. 4.1 (f) and (g). They are visually very close to the results obtained with FUMI, which is based on the full dataset without CS. The FUMI method provides a reference in terms of PSNR, which is understandable since it processes images without CS, while the methods in [23] and [24] provide poor results. Fig. 4.2 displays examples of reconstructed pixel reflectances obtained with the proposed method that can be compared with the method of [29] and FUMI. The advantage of using the LMM can be clearly observed on this example since the reconstructed reflectance obtained with the method of [29] deviates more significantly from the ground truth. On the other hand, the numerical results in Table 4.1 indicate that the proposed method slightly outperforms FUMI even if it uses a reduced amount of data and requires less execution time.

Since the proposed fusion method allows spectral unmixing, it is interesting to analyze the quality of the abundance and endmember estimates. The estimated endmembers are displayed in Fig. 4.3 whereas quantitative results related to unmixing are provided in Table 4.2. The quality of the unmixing results is evaluated using the normalized mean square error of the abundance and endmember matrices (referred to as $\mathrm{NMSE_A}$ and $\mathrm{NMSE_M}$). The spectral distortion of the endmembers is also computed using the spectral angle mapper (SAM) denoted as $\mathrm{SAM_M}$ [58]. These results show that the estimated endmembers are very close to the ground truth even if the fusion has been performed using images with a significant reduced number of measurements. Table 4.2 confirms that the proposed method provides competitive quantitative results with respect to FUMI.

Table 4.1: Performance of MS + HS fusion methods (Jasper dataset): PSNR (dB), UIQI, SAM (degrees), ERGAS, DD ($\times 10^{-2}$), time (seconds) and the data (%)

Methods	PSNR	UIQI	SAM	ERGAS	DD	Time	Data
C-CASSI	39.75	**0.999**	**1.319**	**1.491**	0.492	**12.04**	**50%**
SSCSI	39.22	**0.999**	1.401	1.545	**0.436**	13.58	**50%**
[23]	31.55	0.995	3.103	1.665	1.949	15.75	**50%**
[24]	27.64	0.971	5.875	8.802	4.103	663.3	**50%**
FUMI	**39.76**	0.997	1.933	1.623	0.491	25.81	100%

Table 4.2: Unmixing Performance (Jasper data set): SAM (degrees), $\mathrm{NMSE_M}$ (in Decibels), $\mathrm{NMSE_A}$ (in Decibels)

Methods	$\mathrm{SAM_M}$	$\mathrm{NMSE_M}$	$\mathrm{NMSE_A}$
C-CASSI	**2.7075**	-20.3326	-14.834
SSCSI	2.7127	**-28.6689**	-13.646
FUMI	4.0634	-21.1070	**-18.579**

4.1.2 Urban dataset. In this experiment, the reference image is a section of 128×128 pixels of the Urban HS image [56] [57], whose spectral dimension was subsampled by a

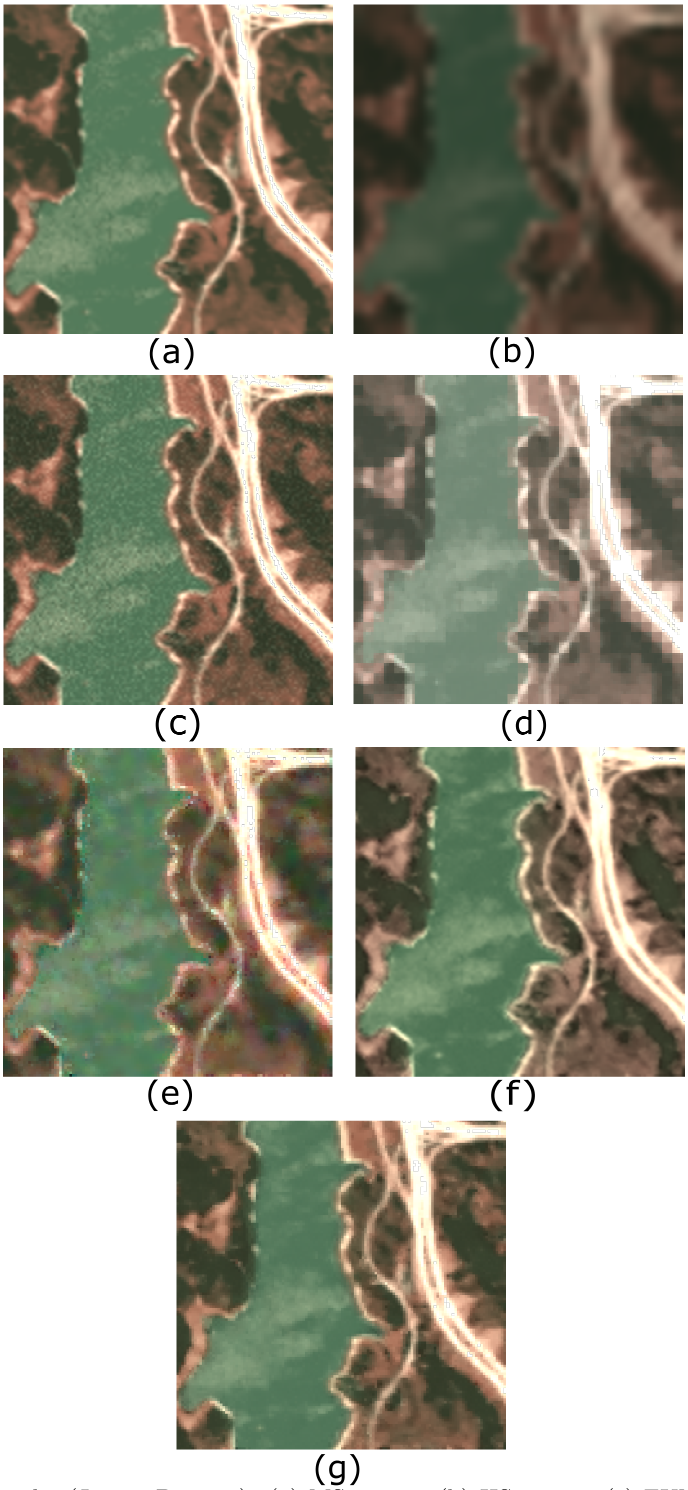

Figure 4.1: Fusion results (Jasper Dataset): (a) MS image. (b) HS image. (c) FUMI (no compression). (d) Method of [23] using the C-CASSI system. (e) [24]. (f) Proposed method with 50% compression using the C-CASSI system. (g) Proposed method with 50% compression using the SSCSI system.

factor of 2 resulting in a reference image of size $128 \times 128 \times 81$. The number of endmembers present in this scene is $p = 6$. Quantitative and qualitative fusion results are presented in Table 4.3 and in Figs. 4.4 and 4.5. Quantitative unmixing results are also reported in

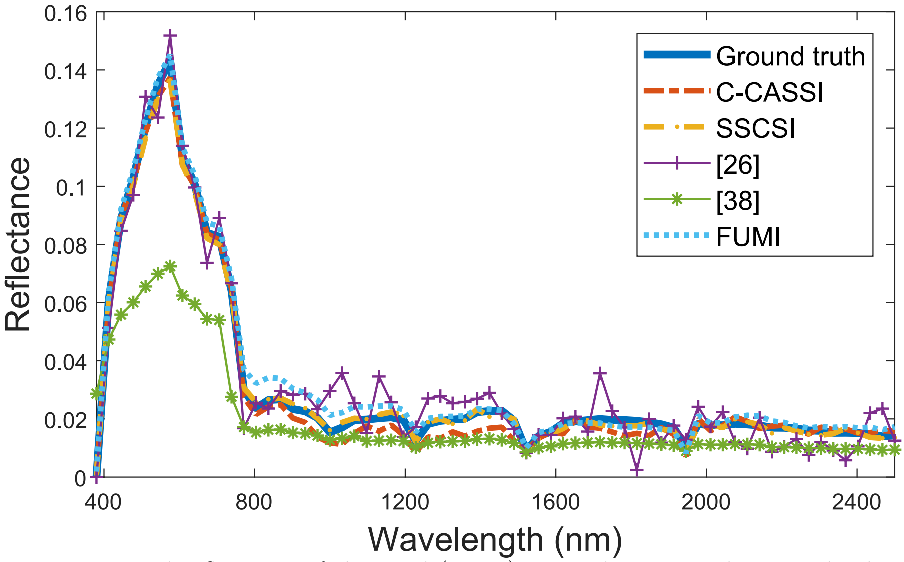

Figure 4.2: Reconstructed reflectance of the pixel $(54, 45)$ using the proposed approach, the methods of [23] and [24] and FUMI, compared to the Jasper ground truth.

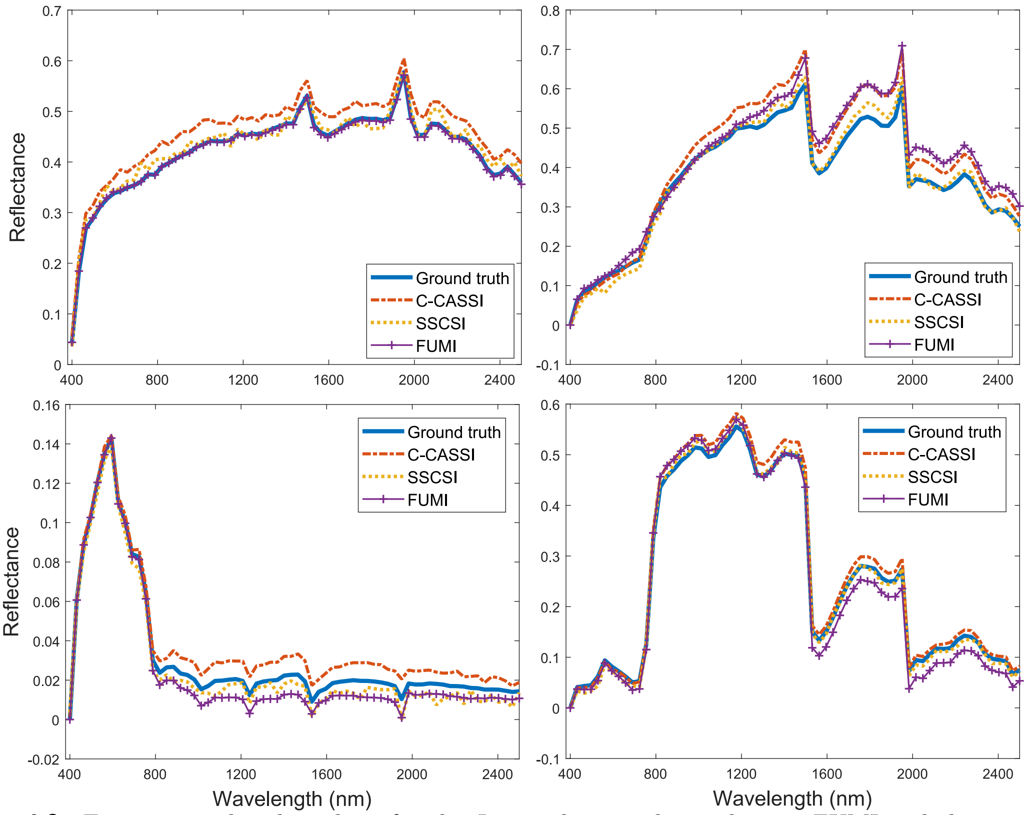

Figure 4.3: Four unmixed endmembers for the Jasper dataset obtained using FUMI and the proposed method with the C-CASSI and SSCSI systems, which are compared to the ground truth.

Table 4.4 whereas the estimated endmembers are shown in Fig. 4.6. Visual results in Fig. 4.4 show that the estimated image is very close to the ground truth. Figs. 4.5 and 4.6 show that the estimated signatures can follow the spectral variations of the ground truth. Moreover, quantitative results reported in Table 4.3 and 4.4 indicate that all performance measures used to evaluate the fusion and unmixing are very satisfactory even if the fusion has been performed using CS images with a significant reduced number of measurements.

Table 4.3: Performance of MS + HS fusion methods (Urban data set): PSNR (dB), UIQI, SAM (degrees), ERGAS, DD ($\times 10^{-2}$), time (seconds) and the data (%)

Methods	PSNR	UIQI	SAM	ERGAS	DD	Time	Data
C-CASSI	**38.04**	**0.997**	**1.810**	1.791	0.518	14.88	**50%**
SSCSI	37.03	0.997	2.083	2.018	**0.512**	17.36	**50%**
[23]	29.04	0.963	2.784	2.472	2.805	15.75	**50%**
FUMI	37.23	0.995	1.815	**1.077**	0.624	**11.87**	100%

Table 4.4: Unmixing Performance (Urban data set): SAM (degrees), $\mathrm{NMSE_M}$ (in Decibels), $\mathrm{NMSE_A}$ (in Decibels)

Methods	$\mathrm{SAM_M}$	$\mathrm{NMSE_M}$	$\mathrm{NMSE_A}$
C-CASSI	**2.2137**	-20.2804	-8.3795
SSCSI	3.1766	**-22.5964**	-8.0117
FUMI	5.6956	-21.5586	**-9.7831**

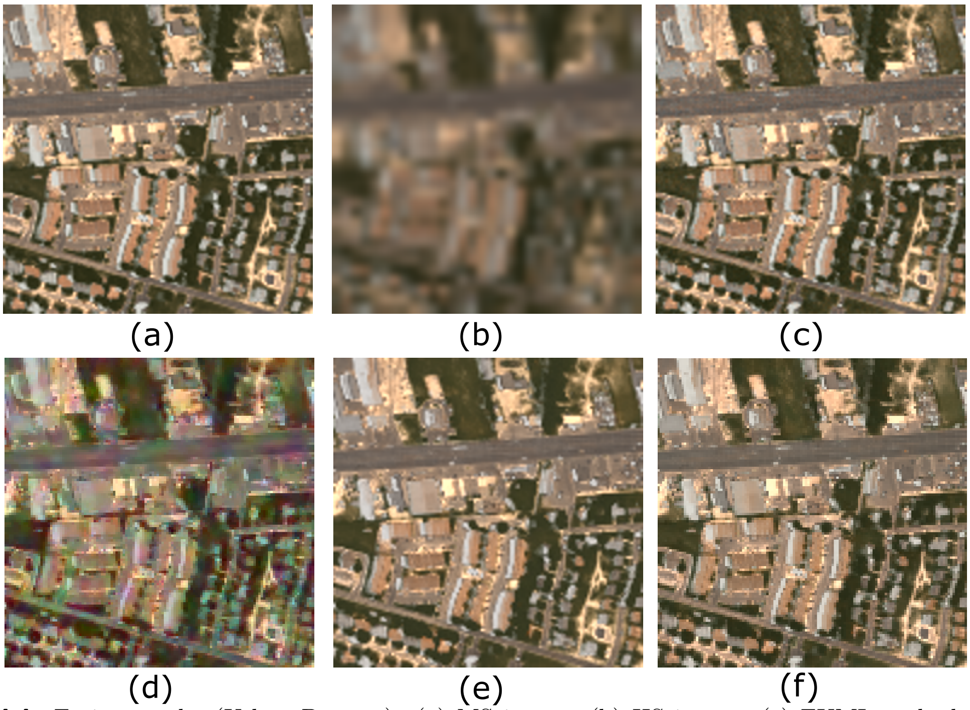

Figure 4.4: Fusion results (Urban Dataset): (a) MS image. (b) HS image. (c) FUMI method with no compression. (d) Method proposed in [23] using the C-CASSI system. (e) Proposed method with 50% compression using the C-CASSI system. (f) Proposed method with 50% compression using the SSCSI system.

4.1.3 Pavia dataset. The reference image used in this last experiment is the scene acquired over Pavia (Northern Italy) by the reflective optics system imaging spectrometer (ROSIS). We worked with a section of the image containing 128 × 128 pixels leading to a reference image of size 128 × 128 × 103. Quantitative and qualitative fusion results are reported in Table 4.5 and Fig. 4.7. The results in Table 4.5 indicate that the proposed

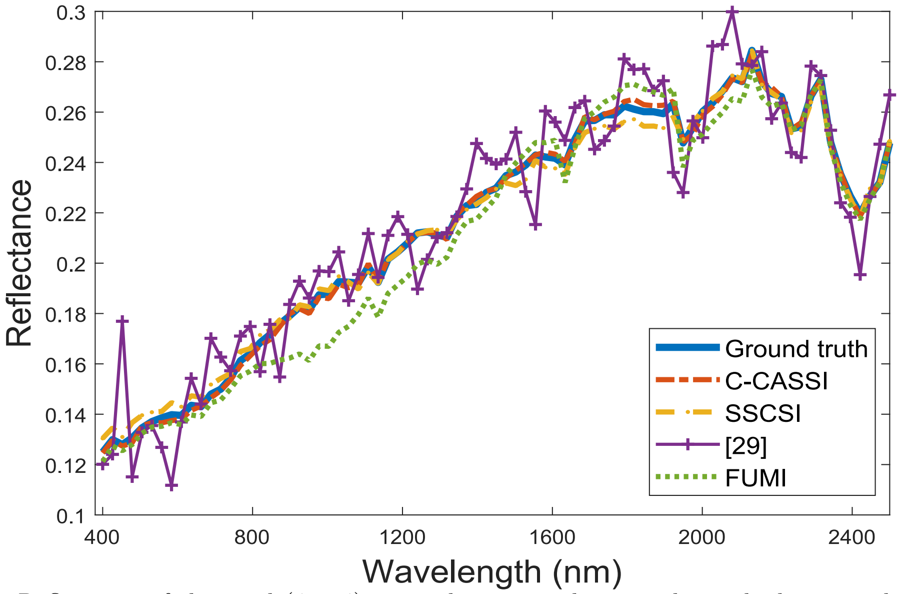

Figure 4.5: Reflectance of the pixel $(45, 54)$ using the proposed approach, method proposed in [23] and FUMI compared to the Urban ground truth.

approach yields a competitive performance when compared to the FUMI method run on the full dataset.

4.1.4 Impact of the compressive ratio.

The last experiments analyze the performance of the proposed algorithm for different numbers of measurements extracted from the Pavia dataset. The PSNRs of the reconstructed images for CASSI and SSCSI as function of the compressive ratio are depicted in Fig. 4.8. They indicate that the accuracy of the recovered images is directly proportional to the amount of data, as expected.

Table 4.5: Performance of MS + HS fusion methods (Pavia data set): PSNR (dB), UIQI, SAM (degrees), ERGAS, DD ($\times 10^{-2}$), time (seconds) and the data (%)

Methods	PSNR	UIQI	SAM	ERGAS	DD	Time	Data
C-CASSI	42.20	**0.996**	2.678	2.832	0.603	**18.23**	**50%**
SSCSI	41.59	0.995	2.807	3.151	0.709	22.49	**50%**
[23]	34.39	0.969	3.141	3.454	1.201	19.48	**50%**
FUMI	**43.34**	0.995	**2.216**	**1.395**	**0.573**	37.64	100%

4.2 Algorithm convergence

In order to illustrate the good convergence of Algorithm 1, a typical evolution of the cost function (3.2) as a function of the iteration number is displayed in Fig. 4.9. The Jasper dataset was used for this experiment and the compressive measurements were simulated with the C-CASSI system with an SNR equal to 30 dB. Fig. 4.9 confirms the fast convergence of the algorithm to a critical point of the objective function, which is here close to 27.73. Note that one iteration of Algorithm 1 includes one iteration of Algorithms 2 and 4. In order to analyze the sensitivity to initialization, we ran the proposed algorithm with 200 different initializations. These initializations were obtained by computing different noisy versions of the endmembers estimated with the method presented in [51]. More precisely, the endmembers resulting from [51] were corrupted by

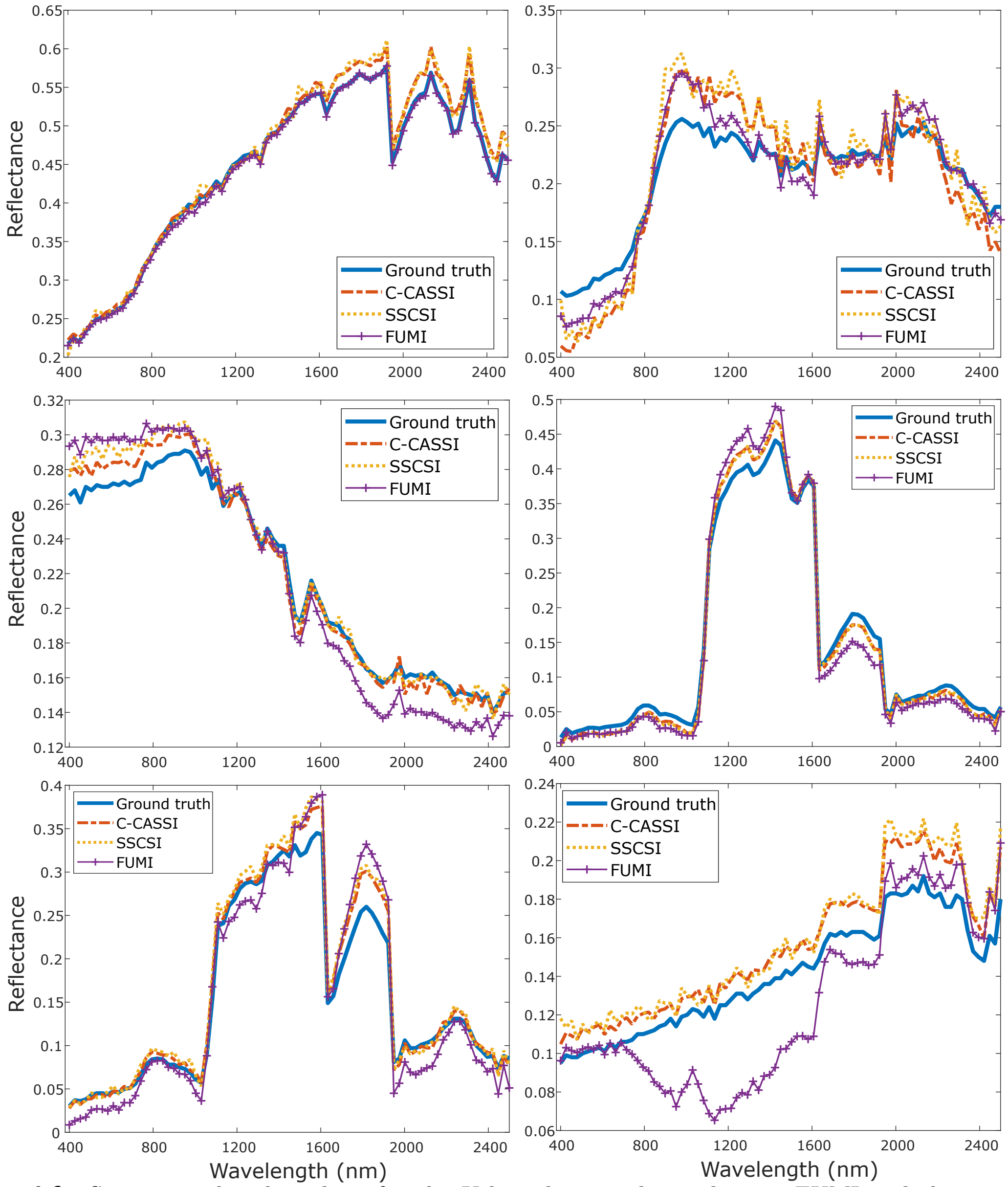

Figure 4.6: Six unmixed endmembers for the Urban dataset obtained using FUMI and the proposed method with C-CASSI and SSCSI systems with a comparison to the ground truth.

different white Gaussian noise sequences with the same SNR equal to 30 dB. The histogram of the corresponding values of the objective function is plotted in Fig. 4.10 showing two different modes, confirming the non-convexity of our fusion problem. Table 4.6 shows quantitative results associated with images corresponding to the two modes of Fig. 4.10 whereas reconstructed images corresponding to these two modes are displayed in Fig. 4.11. These results show that the reconstructed images are visually almost indistinguishable and that the quantitative results are very similar, confirming the good performance of the proposed fusion algorithm.

Figure 4.7: Fusion results (Pavia Dataset): (a) MS image. (b) HS image. (c) FUMI method with no compression. (d) Method proposed in [23] using the C-CASSI system. (e) Proposed method with 50% compression using the C-CASSI system. (f) Proposed method with 50% compression using the SSCSI system.

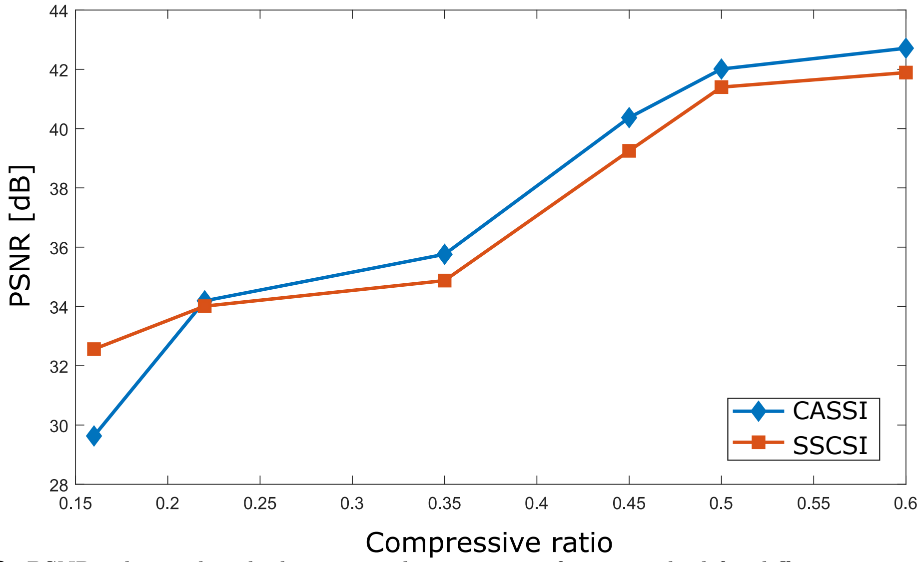

Figure 4.8: PSNRs obtained with the proposed compressive fusion method for different amounts of data for CASSI and SSCSI systems.

Table 4.6: Comparison of the two modes in Jasper data set: Objective function value, PSNR (dB), UIQI, SAM (degrees), ERGAS, DD ($\times 10^{-2}$)

Obj	PSNR	UIQI	SAM	ERGAS	DD
27.727	38.6712	0.999	1.508	1.6634	0.474
28.196	39.6982	0.999	1.341	1.4779	0.426

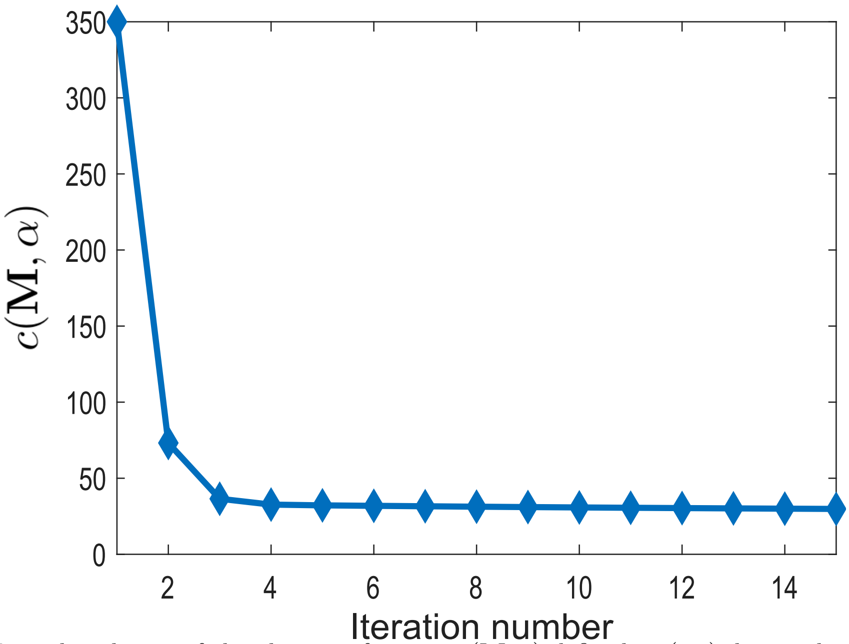

Figure 4.9: Typical evolution of the objective function $c(\mathbf{M}, \alpha)$ defined in (3.2) during the optimization using Algorithm 1.

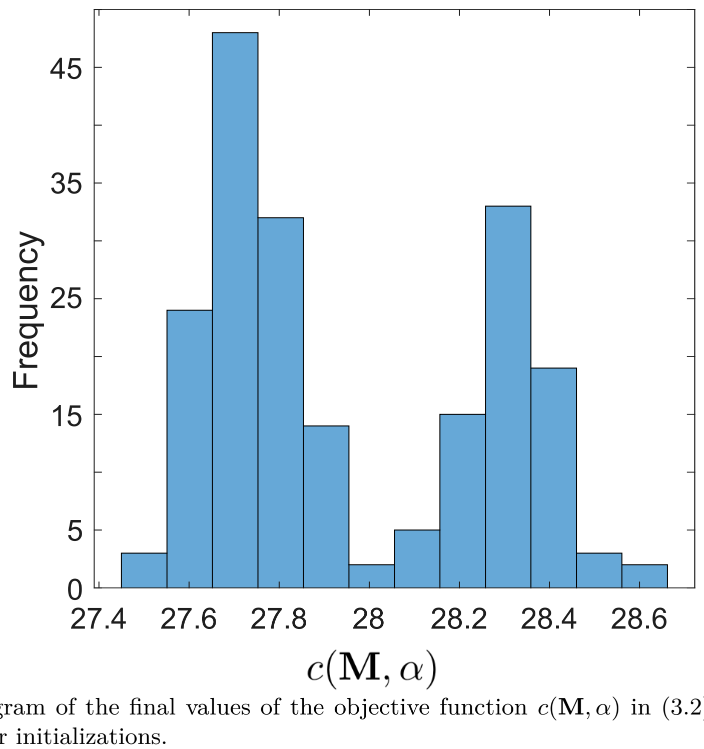

Figure 4.10: Histogram of the final values of the objective function $c(\mathbf{M}, \alpha)$ in (3.2) obtained after 200 different endmember initializations.

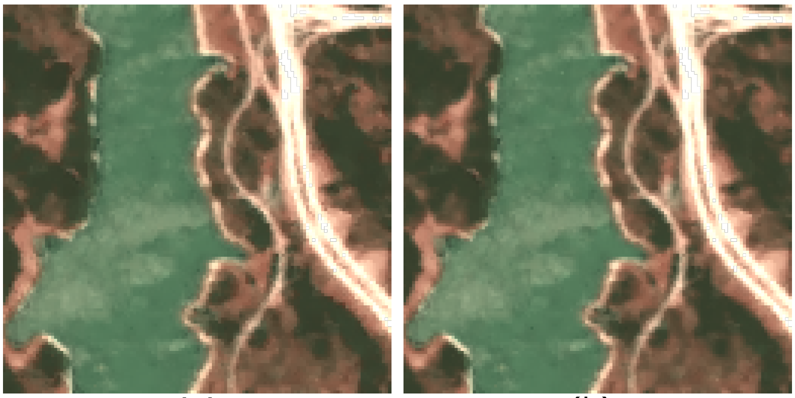

Figure 4.11: Reconstructed images with two different values of the objective function, namely (a) $c(\mathbf{M}, \alpha) = 27.73$ and (b) $c(\mathbf{M}, \alpha) = 28.20$.

5

Conclusions

- This work studied a new fusion algorithm based on spectral unmixing for reconstructing a high-spatial high-spectral image from two compressed multispectral and hyperspectral images.
- A mathematical model for the HS and MS images was developed. The model assumes that the complementary high spatial resolution MS and high spectral resolution HS images result from linear spectral and linear spatial degradations of the target high resolution HS image.
- An optimization problem to recover a high resolution HS image from compressive measurements of HS and MS images has been proposed. The optimization problem includes the linear mixing model in the high resolution HS image, two data fidelity terms corresponding to the MS and HS compressed images, and a regularization function on the abundance maps.
- An iterative algorithm was proposed to solve the formulated optimization problem. The algorithm is an instance of the Block Coordinate Descent algorithm where each block is solved with the alternating direction method of multipliers. The algorithm guarantees the convergence to an stationary point.
- Our results showed that it is possible to recover a high resolution hyperspectral image from compressive spectral imagers, using fewer data samples than using conventional techniques. Further, the algorithm was able to recover good quality of the spectral signatures of the scene even if the information has been compressed.
- Regularization parameters were estimated by cross-validation in this work. It would be also interesting to study methods allowing these parameters to be estimated directly from the data such as the methods investigated in [59].

A

Endmember Initialization

A.1 Endmember Initialization

In this section we detailed describe the strategy used to estimate the initial guest of the endmembers. We introduce an equivalent observation model of CSI systems and an orthogonal formulation in order to include the Rayleigh-Ritz procedure in the context of CSI acquisition model. We consider the following equivalent model for the observed compressive hyperspectral image

$$\mathbf{Y} = \mathbf{H}\mathbf{X} \tag{A.1}$$

where $\mathbf{X} \in \mathbb{R}^{L \times N}$ is the hyperspectral image, with L as the number of spectral bands and N as the number of pixels; $\mathbf{H} \in \mathbb{R}^{M \times L}$ models the sensing process; and $\mathbf{Y} \in \mathbb{R}^{M \times N}$ represents the acquired data, where M is the number of measurements. In a CS scenario, it is assumed that $M \ll L$. In (A.1) we consider that $\mathbf{X} = [\mathbf{x}_1, \cdots, \mathbf{x}_N]$, where each column $\mathbf{x}_i$ is the spectral signature of a pixel of the hyperspectral image. This equivalent formulation can be achieved under the assumption that every spectral pixel is captured in all snapshots with all available filters. In practical applications the number of optical filters are limited, thus this assumption is easily satisfied.

A.1.1 Compressive Orthogonal Random Projections.

Based on the acquisition model introduced in (A.1), and taking into account the singular value decomposition (SVD) of the matrix $\mathbf{H}$, one can obtain that

$$\mathbf{Y} = (\mathbf{U}\mathbf{D}\mathbf{V}^T)\mathbf{X}, \tag{A.2}$$

where $\mathbf{H} = \mathbf{U}\mathbf{D}\mathbf{V}^T$, $\mathbf{U} \in \mathbb{R}^{M \times M}$, $\mathbf{V} \in \mathbb{R}^{L \times L}$ satisfy that $\mathbf{U}^T\mathbf{U} = \mathbf{I}_M$, $\mathbf{V}\mathbf{V}^T = \mathbf{I}_L$, and $\mathbf{D} \in \mathbb{R}^{M \times L}$ is a diagonal matrix. Note that, given that $M \ll L$, the matrix $\mathbf{H}$ is rank deficient, which implies that the inverse problem concerning to estimate $\mathbf{X}$ is an ill-posed problem [60]. Thus, in order to solve this limitation we first estimate the closest full column rank approximation to the matrix $\mathbf{H}$. Specifically, we consider the following lemma for calculating the full column rank approximation of the matrix $\mathbf{H}$.

Lemma A.1.1. *Define $r = rank(\mathbf{H})$, with $r \leq M$. Then, the best low rank approximation of the matrix $\mathbf{H}$ is the following truncated matrix*

$$\tilde{\mathbf{H}} = \tilde{\mathbf{U}}\tilde{\mathbf{D}}\tilde{\mathbf{V}}^T, \tag{A.3}$$

where $\tilde{\mathbf{U}} \in \mathbb{R}^{M\times r}$ *is the matrix* $\mathbf{U}$ *in* (A.2) *with the last* $M-r$ *columns removed,* $\tilde{\mathbf{V}} \in \mathbb{R}^{L\times r}$ *is the matrix* $\mathbf{V}$ *in* (A.2) *with the last* $(L-r)$ *columns removed, and* $\tilde{\mathbf{D}} \in \mathbb{R}^{r\times r}$ *is a diagonal matrix, where its entries are given by the first* r *entries in the main diagonal of* $\mathbf{D}$ *in* (A.2)*.*

Proof. The proof of this lemma is developed in [61]. □

Considering the full column rank closest approximation established in Lemma A.1.1, we can equivalently approximate the measurements in (A.1) as

$$\tilde{\mathbf{Y}} = \tilde{\mathbf{D}}\mathbf{U}^T\mathbf{Y} = \tilde{\mathbf{V}}^T\mathbf{X}, \tag{A.4}$$

The main motivation for considering this approximated system in (A.4) is that this provides a link between the Rayleigh-Ritz theory and CSI model. Considering the system (A.4), it can be observed that

$$\tilde{\mathbf{Y}}\tilde{\mathbf{Y}}^T/N = \tilde{\mathbf{V}}^T\mathbf{X}\mathbf{X}^T\tilde{\mathbf{V}}/N = \tilde{\mathbf{V}}^T\mathbf{\Sigma}\tilde{\mathbf{V}}, \tag{A.5}$$

where $\mathbf{\Sigma}$ represents the covariance matrix of the dataset $\mathbf{X}$. Notice that $\mathbf{X}\mathbf{X}^T = \mathbf{\Sigma}$ is valid when the dataset has zero mean. Further, it is worth nothing that taking $\mathbf{A} = \mathbf{\Sigma}$, and $\mathbf{B} = \tilde{\mathbf{V}}$, the matrix $\tilde{\mathbf{Y}}\tilde{\mathbf{Y}}^T/N$ in (A.5) represents the matrix $\mathbf{R}$ in the Rayleigh-Ritz procedure summarized in Section 2.6. According to Theorem 2.6.1, the eigenvectors of $\mathbf{\Sigma}$, which are the basis of the subspace in which the dataset $\mathbf{X}$ lies, can be approximated using the pairs $(\tilde{\lambda}_i, \mathbf{u}_i)$ yielded by the Rayleigh-Ritz procedure. The next section introduces a recent technique based on Principal Component Analysis (PCA) to estimate eigenvectors of the covariance matrix $\mathbf{\Sigma}$ using the Ritz vectors.

A.1.2 Signal Subspace Estimation. This section presents a procedure to estimate the finite dimensional space in which the sensed hyperspectral image $\mathbf{X}$ belongs. In fact, in order to take advantage of the statistical relationship between the covariance matrix of the data $\mathbf{\Sigma}$ and the measurements in (A.5), we use the Compressive-Projection Principal Component Analysis (CPPCA) technique developed in [62] to estimate the eigenvectors from compressive measurements explained as follows.

A.1.3 CPPCA procedure. First, we aim at estimating the eigendecomposition of the covariance matrix $\mathbf{\Sigma}$ from the approximated measurements $\tilde{\mathbf{Y}}$ in (A.4). To do that, first consider the covariance matrix $\mathbf{\Sigma} = \mathbf{W}\mathbf{\Lambda}\mathbf{W}^T$ such that $\mathbf{W} = [\mathbf{w}_1, \cdots, \mathbf{w}_L]$, and $\mathbf{w}_i$, for $i = 1, \cdots, N$ are the unit eigenvectors. Then, consider a fixed eigenvector $\mathbf{w}_k$. Given the fact that matrix $\tilde{\mathbf{V}}$ is orthogonal, then the orthogonal projector to the generated subspace $\mathcal{P}$ by the matrix $\tilde{\mathbf{V}}$ is given by $\tilde{\mathbf{V}}\tilde{\mathbf{V}}^T$ [46]. Thus, the normalized orthogonal projection of $\mathbf{w}_k$ onto $\mathcal{P}$ is given by

$$\mathbf{v}_k = \frac{\tilde{\mathbf{V}}\tilde{\mathbf{V}}^T\mathbf{w}_k}{\|\tilde{\mathbf{V}}\tilde{\mathbf{V}}^T\mathbf{w}_k\|_2}. \tag{A.6}$$

Then, considering (A.6), in the CPPCA approach is observed that building an auxiliary subspace $\mathcal{Q}$ given by

$$\mathcal{Q}_k = \mathcal{P}^{\perp} \oplus \operatorname{span}(\mathbf{v}_k), \tag{A.7}$$

contains the eigenvector $\mathbf{w}_k$ [62], *i.e.* $\mathbf{w}_k \in \mathcal{Q}_k$, where $\mathcal{P}^{\perp}$ denotes the orthogonal complement of $\mathcal{P}$. Moreover, according to the sensing process in (A.4) we can split the dataset $\mathbf{X} = [\mathbf{x}_1, \mathbf{x}_2, \cdots, \mathbf{x}_N]$ into J partitions $\mathbf{X}^{(j)}$ each one associated with its own randomly chosen projection $\tilde{\mathbf{V}}^{(j)}$, for $j = 1, \cdots, J$. We assume that the splitted dataset is separated such that each $\mathbf{X}^{(j)}$ closely resembles the whole dataset $\mathbf{X}$ statistically and so it has approximately the same eigendecomposition [63, 64]. Thus, forming the corresponding subspaces $\mathcal{Q}_k^{(j)}$ for each partition (j) via (A.7) it can be concluded that $\mathbf{w}_k \in \mathcal{Q}_k^{(1)} \cap \cdots \cap \mathcal{Q}_k^{(J)}$. Since we do not have knowledge about the normalized projections $\mathbf{v}_k^{(j)}$, under the assumption that eigenvalue $\lambda_k(\boldsymbol{\Sigma})$ is sufficiently separated in value with respect to the other ones, we can use the Ritz vectors $\mathbf{u}_k^{(j)}$ to approximate $\mathbf{v}_k^{(j)}$ and form the spaces $\mathcal{Q}_k^{(j)}$ [62]. Considering these conditions and due to $\mathcal{Q}_k^{(j)}$ are convex and closed, a projection onto convex set optimization can be used to approximate $\mathbf{W}$. Thus, iteratively the eigenvector $\mathbf{w}_k$ can be approximated as

$$\hat{\mathbf{w}}_k^{(i)} = \frac{1}{J} \sum_{j=1}^{J} \mathbf{Q}_k^{(j)} \mathbf{Q}_k^{(j)^T} \hat{\mathbf{w}}_k^{(i-1)}, \tag{A.8}$$

where i is the iteration index, the projection onto $\mathcal{Q}^{(j)}$ is performed by the matrix $\mathbf{Q}_k^{(j)} = \left[\mathbf{u}_k^{(j)}, \mathbf{I} - \tilde{\mathbf{V}}^{(j)} \tilde{\mathbf{V}}^{(j)T}\right] \in \mathbb{R}^{L \times (L+1)}$, and CPPCA initializes $\hat{\mathbf{w}}_k^{(0)}$ to the average of the Ritz vectors [62]. The iterations in (A.8) converges to $\hat{\mathbf{w}}_k$ which after appropriate normalization will approximate the desired eigenvector $\mathbf{w}_k$ (up to sign) [62]. Finally, we note that a limitation of CPPCA is given by the fact that the Rayleigh-Ritz method requires well separated eigenvalues, which in HS images is true for the first largest eigenvalues.

A.1.4 Endmember Estimation Algorithm. This final section presents the proposed algorithm for estimating the endmembers from compressive measurements. Algorithm 6 summarizes the proposed procedure. First, Algorithm 6 estimates the measurements of the CSI system using the approximation defined in (A.4). Second, the basis of the signal subspace (*i.e.* $\hat{\mathbf{W}}_d$) is estimate from the first d columns of $\hat{\mathbf{W}}$ using the CPPCA procedure. For the sake of completeness of the proposed approach, CPPCA procedure is described in Algorithm 7. CPPCA computes the corresponding PCA coefficients using the pseudoinverse $\mathbf{Z}^{(j)} = (\tilde{\mathbf{V}}^{(j)T} \hat{\mathbf{W}}_d)^{+} \tilde{\mathbf{Y}}^{(j)}$. Finally, the VCA procedure is performed to the subspace previously identified. Here, we note that if we project the cone C_p, which lie in a subspace of dimension p in a subspace $E_d \supset E_p$, followed by a projection in a properly hyperplane, the projection is still a simplex with the same vertices that S_p.

Algorithm 6: Endmember Estimation Algorithm

1: **Input:** $\mathbf{Y} \in \mathbb{R}^{M \times N}$, $\mathbf{H} \in \mathbb{R}^{M \times L}$. Choose the number of partitions J.
2: $\tilde{\mathbf{H}} = \tilde{\mathbf{U}} \tilde{\mathbf{D}} \tilde{\mathbf{V}}^T$ (A.2)
3: $\tilde{\mathbf{Y}} = \tilde{\mathbf{V}}^T \mathbf{X}$ (A.4)
4: $\hat{\mathbf{W}} \leftarrow \text{CPPCA}(\tilde{\mathbf{Y}}, \tilde{\mathbf{V}}, J)$ Algorithm 7
5: $\hat{\mathbf{M}} \leftarrow \text{VCA}(\hat{\mathbf{W}}_d, \tilde{\mathbf{Y}})$ Algorithm in [31]
6: **Return** $\hat{\mathbf{M}}$

Algorithm 7: CPPCA Procedure [62]

Input: $\tilde{\mathbf{Y}}, \tilde{\mathbf{V}}, J$
Choose $\left\{\mathbf{X}^{(1)}, \mathbf{X}^{(2)}, \cdots, \mathbf{X}^{(J)}\right\}$
Determine $\left\{\tilde{\mathbf{V}}^{(1)}, \cdots, \tilde{\mathbf{V}}^{(J)}\right\}$
Set: $\left\{\tilde{\mathbf{Y}}^{(j)} = \tilde{\mathbf{V}}^{(j)^T}\mathbf{X}^{(j)} | \quad j = 1, \cdots, J\right\}$
Estimate the Ritz vectors $\left\{\mathbf{u}_k^{(j)} | \quad k = 1, \cdots, L, \;\; j = 1, \cdots, J\right\}$ of the L eigenvectors $\mathbf{w}_k$ of the matrix $\tilde{\mathbf{\Sigma}}^{(j)}$, according to Section 2.6. (A.5)
$\mathbf{P}^{(j)\perp} = \mathbf{I} - \tilde{\mathbf{V}}^{(j)}\tilde{\mathbf{V}}^{(j)^T}$
for $k = 1 : L$ **do**
  $\mathbf{Q}_k^{(j)} = \left[\mathbf{u}_k^{(j)}, \mathbf{P}^{(j)\perp}\right]$ (A.7)
  $\hat{\mathbf{w}}_k^{(0)} = \frac{1}{JL}\sum_{k,j}\mathbf{u}_k^{(j)}$.
  for $i = 1 : T$ **do**
    $\hat{\mathbf{w}}_k^{(i)} = \frac{1}{J}\sum_{j=1}^{J}\mathbf{Q}_k^{(j)}\mathbf{Q}_k^{(j)^T}\hat{\mathbf{w}}_k^{(i-1)}$ (A.8)
  end for
end for
Return $\hat{\mathbf{W}} = [\hat{\mathbf{w}}_1, \cdots, \hat{\mathbf{w}}_L]$

Bibliography

[1] S. M. Hsu and H.-H. K. Burke, "Multisensor fusion with hyperspectral imaging data: detection and classification," *Lincoln Laboratory Journal*, vol. 14, no. 1, 2003.

[2] M. E. Schaepman, S. L. Ustin, A. J. Plaza, T. H. Painter, J. Verrelst, and S. Liang, "Earth system science related imaging spectroscopy-An assessment," *Remote Sens. Environ.*, vol. 113, no. 123–137, 2009.

[3] S. V. Panasyuk, S. Yang, D. V. Faller, D. Ngo, R. A. Lew, J. E. Freeman, and A. E. Rogers, "Medical hyperspectral imaging to facilitate residual tumor identification during surgery," *Cancer biology & therapy*, vol. 6, no. 3, pp. 439–446, 2007.

[4] N. F. Schreiber, R. Genzel, N. Bouché, G. Cresci, R. Davies, P. Buschkamp, K. Shapiro, L. Tacconi, E. Hicks, S. Genel, *et al.*, "The SINS survey: SINFONI integral field spectroscopy of z 2 star-forming galaxies," *The Astrophysical Journal*, vol. 706, no. 2, p. 1364, 2009.

[5] G. A. Shaw and H.-H. K. Burke, "Spectral imaging for remote sensing," *Lincoln Laboratory Journal*, vol. 14, no. 1, pp. 3–28, 2003.

[6] S. K. Sahoo, D. Tang, and C. Dang, "Single-shot multispectral imaging with a monochromatic camera," *Optica*, vol. 4, no. 10, pp. 1209–1213, 2017.

[7] T. Caras, J. Hedley, and A. Karnieli, "Implications of sensor design for coral reef detection: Upscaling ground hyperspectral imagery in spatial and spectral scales," *International Journal of Applied Earth Observation and Geoinformation*, vol. 63, pp. 68–77, 2017.

[8] E. M. Middleton, S. G. Ungar, D. J. Mandl, L. Ong, S. W. Frye, P. E. Campbell, D. R. Landis, J. P. Young, and N. H. Pollack, "The Earth Observing One (EO-1) satellite mission: Over a decade in space," *IEEE J. Sel. Topics Appl. Earth Observ. in Remote Sens.*, vol. 6, no. 2, pp. 243–256, 2013.

[9] S. Foucart and H. Rauhut, *A mathematical introduction to compressive sensing*, vol. 1. Birkhäuser Basel, 2013.

[10] M. Gehm, R. John, D. Brady, R. Willett, and T. Schulz, "Single-shot compressive spectral imaging with a dual-disperser architecture," *Optics Express*, vol. 15, no. 21, pp. 14013–14027, 2007.

[11] M. F. Duarte, M. A. Davenport, D. Takbar, J. N. Laska, T. Sun, K. F. Kelly, and R. G. Baraniuk, "Single-pixel imaging via compressive sampling," *IEEE Signal Process. Mag*, vol. 25, no. 2, pp. 83–91, 2008.

[12] C. V. Correa, C. A. Hinojosa, G. R. Arce, and H. Arguello, "Multiple snapshot colored compressive spectral imager," *Optical Engineering*, vol. 56, no. 4, p. 041309, 2016.

[13] G. R. Arce, D. J. Brady, L. Carin, H. Arguello, and D. S. Kittle, "Compressive coded aperture spectral imaging: An introduction," *IEEE Signal Process. Mag.*, vol. 31, no. 1, pp. 105–115, 2014.

[14] H. Arguello and G. Arce, "Spectrally Selective Compressive Imaging by Matrix System Analysis," in *Imaging Appl. Opt. Tech. Pap.*, (Washington, D.C.), OSA, June 2012.

[15] H. J. Kramer, *Observation of the Earth and its Environment: Survey of Missions and Sensors.* Springer Science & Business Media, 2002.

[16] Q. Wei, J. Bioucas-Dias, N. Dobigeon, and J.-Y. Tourneret, "Hyperspectral and multispectral image fusion based on a sparse representation," *IEEE Trans. Geosci. Remote Sens*, vol. 53, no. 7, pp. 3658–3668, 2015.

[17] M. Simões, J. Bioucas-Dias, L. B. Almeida, and J. Chanussot, "A convex formulation for hyperspectral image superresolution via subspace-based regularization," *IEEE Trans. Geosci. Remote Sens.*, vol. 53, no. 6, pp. 3373–3388, 2015.

[18] L. Loncan, L. B. de Almeida, J. M. Bioucas-Dias, X. Briottet, J. Chanussot, N. Dobigeon, S. Fabre, W. Liao, G. A. Licciardi, M. Simoes, *et al.*, "Hyperspectral pansharpening: A review," *IEEE Geosci. Remote Sens. Mag.*, vol. 3, no. 3, pp. 27–46, 2015.

[19] G. Vivone, L. Alparone, J. Chanussot, M. Dalla Mura, A. Garzelli, G. A. Licciardi, R. Restaino, and L. Wald, "A critical comparison among pansharpening algorithms," *IEEE Trans. Geosci. Remote Sens.*, vol. 53, no. 5, pp. 2565–2586, 2015.

[20] B. Zhukov, D. Oertel, F. Lanzl, and G. Reinhackel, "Unmixing-based multisensor multiresolution image fusion," *IEEE Trans. Geosci. Remote Sens.*, vol. 37, no. 3, pp. 1212–1226, 1999.

[21] Q. Wei, J. Bioucas-Dias, N. Dobigeon, J.-Y. Tourneret, M. Chen, and S. Godsill, "Multiband image fusion based on spectral unmixing," *IEEE Trans. Geosci. Remote Sens*, vol. 54, no. 12, pp. 7236–7249, 2016.

[22] N. Yokoya, T. Yairi, and A. Iwasaki, "Coupled nonnegative matrix factorization unmixing for hyperspectral and multispectral data fusion," *IEEE Trans. Geosci. Remote Sens.*, vol. 50, no. 2, pp. 528–537, 2012.

[23] E. Vargas, O. Espitia, H. Arguello, and J.-Y. Tourneret, "Spectral image fusion from compressive measurements," *submitted to IEEE Trans. Image Process.*, 2018.

[24] T. Wan, N. Canagarajah, and A. Achim, "Compressive image fusion," in *Proc. Int. Conf. Image Process. (ICIP 2008)*, (San Diego, CA, USA), pp. 1308–1311, Oct. 2008.

[25] H. Arguello and G. R. Arce, "Colored coded aperture design by concentration of measure in compressive spectral imaging," *IEEE Trans. Image Process.*, vol. 23, no. 4, pp. 1896–1908, 2014.

[26] X. Lin, Y. Liu, J. Wu, and Q. Dai, "Spatial-spectral encoded compressive hyperspectral imaging," *ACM Transactions on Graphics (TOG)*, vol. 33, no. 6, p. 233, 2014.

[27] H. Rueda, H. Arguello, and G. R. Arce, "Dmd-based implementation of patterned optical filter arrays for compressive spectral imaging," *JOSA A*, vol. 32, no. 1, pp. 80–89, 2015.

[28] H. Arguello and G. R. Arce, "Rank minimization code aperture design for spectrally selective compressive imaging," *IEEE Trans. Image Process.*, vol. 22, no. 3, pp. 941–954, 2013.

[29] I. August, Y. Oiknine, M. AbuLeil, I. Abdulhalim, and A. Stern, "Miniature compressive ultra-spectral imaging system utilizing a single liquid crystal phase retarder," *Scientific reports*, vol. 6, p. 23524, 2016.

[30] N. Keshava and J. F. Mustard, "Spectral unmixing," *IEEE Signal Process. Mag.*, vol. 19, no. 1, pp. 44–57, 2002.

[31] J. M. Nascimento and J. M. Dias, "Vertex component analysis: A fast algorithm to unmix hyperspectral data," *IEEE Trans. Geosci. Remote Sens.*, vol. 43, no. 4, pp. 898–910, 2005.

[32] T.-H. Chan, W.-K. Ma, A. Ambikapathi, and C.-Y. Chi, "A simplex volume maximization framework for hyperspectral endmember extraction," *IEEE Trans. Geosci. Remote Sens.*, vol. 49, no. 11, pp. 4177–4193, 2011.

[33] M. E. Winter, "N-FINDR: An algorithm for fast autonomous spectral end-member determination in hyperspectral data," in *Proc. SPIE's International Symposium on Optical Science, Engineering, and Instrumentation*, (Denver, CO, USA), pp. 266–275, 1999.

[34] V. Backman, M. B. Wallace, L. Perelman, J. Arendt, R. Gurjar, M. Müller, Q. Zhang, G. Zonios, E. Kline, T. McGillican, *et al.*, "Detection of preinvasive cancer cells," *Nature*, vol. 406, no. 6791, p. 35, 2000.

[35] S. Delalieux, A. Auwerkerken, W. W. Verstraeten, B. Somers, R. Valcke, S. Lhermitte, J. Keulemans, and P. Coppin, "Hyperspectral reflectance and fluorescence imaging to detect scab induced stress in apple leaves," *Remote Sensing*, vol. 1, no. 4, pp. 858–874, 2009.

[36] R. T. Kester, N. Bedard, L. Gao, and T. S. Tkaczyk, "Real-time snapshot hyperspectral imaging endoscope," *Journal of biomedical optics*, vol. 16, no. 5, pp. 056005–056005, 2011.

[37] A. Gowen, C. O'Donnell, P. Cullen, G. Downey, and J. Frias, "Hyperspectral imaging–an emerging process analytical tool for food quality and safety control," *Trends in Food Science & Technology*, vol. 18, no. 12, pp. 590–598, 2007.

[38] R. O. Green, M. L. Eastwood, C. M. Sarture, T. G. Chrien, M. Aronsson, B. J. Chippendale, J. A. Faust, B. E. Pavri, C. J. Chovit, M. Solis, *et al.*, "Imaging spectroscopy and the airborne visible/infrared imaging spectrometer (aviris)," *Remote sensing of environment*, vol. 65, no. 3, pp. 227–248, 1998.

[39] E. Herrala, J. Okkonen, T. Hyvarinen, M. Aikio, and J. Lammasniemi, "Imaging spectrometer for process industry applications," in *Proc. SPIE*, vol. 2248, pp. 33–40, 1994.

[40] H. R. Morris, C. C. Hoyt, and P. J. Treado, "Imaging spectrometers for fluorescence and raman microscopy: acousto-optic and liquid crystal tunable filters," *Applied spectroscopy*, vol. 48, no. 7, pp. 857–866, 1994.

[41] E. J. Candès and M. B. Wakin, "An introduction to compressive sampling," *IEEE signal processing magazine*, vol. 25, no. 2, pp. 21–30, 2008.

[42] A. Wagadarikar, R. John, R. Willett, and D. Brady, "Single disperser design for coded aperture snapshot spectral imaging," *Applied optics*, vol. 47, no. 10, pp. B44–B51, 2008.

[43] C. V. Correa, H. Arguello, and G. R. Arce, "Snapshot colored compressive spectral imager," *JOSA A*, vol. 32, no. 10, pp. 1754–1763, 2015.

[44] N. Yokoya, C. Grohnfeldt, and J. Chanussot, "Hyperspectral and multispectral data fusion: A comparative review of the recent literature," *IEEE Geoscience and Remote Sensing Magazine*, vol. 5, no. 2, pp. 29–56, 2017.

[45] J. M. Bioucas-Dias, A. Plaza, N. Dobigeon, M. Parente, Q. Du, P. Gader, and J. Chanussot, "Hyperspectral unmixing overview: Geometrical, statistical, and sparse regression-based approaches," *IEEE J. Sel. Top. Appl. Earth Obs. Remote Sens.*, vol. 5, no. 2, pp. 354–379, 2012.

[46] B. N. Parlett, *The symmetric eigenvalue problem*, vol. 20. siam, 1998.

[47] Q. Wei, N. Dobigeon, and J.-Y. Tourneret, "Bayesian fusion of multi-band images," *IEEE J. Sel. Topics Signal Process.*, vol. 9, no. 6, pp. 1117–1127, 2015.

[48] Y. Wang, J. Yang, W. Yin, and Y. Zhang, "A new alternating minimization algorithm for total variation image reconstruction," *SIAM Journal on Imaging Sciences*, vol. 1, no. 3, pp. 248–272, 2008.

[49] D. P. Bertsekas, *Nonlinear programming.* Belmont, MA, USA: Athena scientific, 1999.

[50] S. Boyd, N. Parikh, E. Chu, B. Peleato, and J. Eckstein, "Distributed optimization and statistical learning via the alternating direction method of multipliers," *Foundations and Trends® in Machine Learning*, vol. 3, no. 1, pp. 1–122, 2011.

[51] E. Vargas, S. Pinilla, and H. Arguello, "A fast endmember estimation algorithm from compressive measurements," in *Proc. European Signal Process. Conf. (EUSIPCO)*, (Roma, Italy), Oct. 2018.

[52] M. Marquez, Y. Mejia, and H. Arguello, "Compressive spectral image super-resolution by using singular value decomposition," *Optics Communications*, vol. 404, pp. 163–168, 2017.

[53] S. Boyd and L. Vandenberghe, *Convex optimization.* Cambridge, U.K.: Cambridge University Press, 2004.

[54] P. Tseng, "Convergence of a block coordinate descent method for nondifferentiable minimization," *Journal of optimization theory and applications*, vol. 109, no. 3, pp. 475–494, 2001.

[55] Á. Barbero and S. Sra, "Modular proximal optimization for multidimensional total-variation regularization," *ArXiv e-prints*, Nov. 2014.

[56] F. Zhu, Y. Wang, S. Xiang, B. Fan, and C. Pan, "Structured sparse method for hyperspectral unmixing," *ISPRS Journal of Photogrammetry and Remote Sensing*, vol. 88, pp. 101–118, 2014.

[57] F. Zhu, Y. Wang, B. Fan, G. Meng, S. Xiang, and C. Pan, "Spectral unmixing via data-guided sparsity," *IEEE Trans. Image Process.*, vol. 23, no. 12, pp. 5412–5427, 2014.

[58] P. E. Dennison, K. Q. Halligan, and D. A. Roberts, "A comparison of error metrics and constraints for multiple endmember spectral mixture analysis and spectral angle mapper," *Remote Sensing of Environment*, vol. 93, no. 3, pp. 359–367, 2004.

[59] M. Pereyra, P. Schniter, E. Chouzenoux, J.-C. Pesquet, J.-Y. Tourneret, A. Hero, and S. McLaughlin, "Tutorial on stochastic simulation and optimization methods in signal processing," *IEEE J. Sel. Topics Signal Process.*, vol. 10, pp. 224–241, Mar. 2016.

[60] A. Tikhonov, *Numerical methods for the solution of ill-posed problems.*

[61] G. H. Golub, A. Hoffman, and G. W. Stewart, "A generalization of the eckart-young-mirsky matrix approximation theorem," *Linear Algebra and its applications*, vol. 88, pp. 317–327, 1987.

[62] J. E. Fowler, "Compressive-projection principal component analysis," *IEEE Trans. Image Process.*, vol. 18, no. 10, pp. 2230–2242, 2009.

[63] B. Penna, T. Tillo, E. Magli, and G. Olmo, "A new low complexity klt for lossy hyperspectral data compression," in *Geoscience and Remote Sensing Symposium, 2006. IGARSS 2006. IEEE International Conference on*, pp. 3525–3528, IEEE, 2006.

[64] Q. Du and J. E. Fowler, "Low-complexity principal component analysis for hyperspectral image compression," *The International Journal of High Performance Computing Applications*, vol. 22, no. 4, pp. 438–448, 2008.